Polar Science 46 (2025) 101256

Contents lists available at ScienceDirect

Polar Science

journal homepage: www.elsevier.com/locate/polar

Diurnal variation of the planetary boundary layer over Dome C (Antarctica) impacting the formation of supercooled liquid water clouds

Philippe Ricaud [a,*], Pierre Durand [b], Paolo Grigioni [c], Virginia Ciardini [c], Massimo Del Guasta [d], Giuseppe Camporeale [e], Jean-Luc Attié [b], Eric Bazile [a]

[a] CNRM, Université de Toulouse, Météo-France, CNRS, Toulouse, France
[b] Laboratoire D'Aérologie, Université de Toulouse, CNRS, Toulouse, France
[c] ENEA, Roma, Italy
[d] INO-CNR, Sesto Fiorentino, Italy
[e] IREA-CNR, Bari, Italy

A B S T R A C T

While the majority of Antarctic clouds are made up of ice crystals, a significant proportion consists of supercooled liquid water (SLW), defined as water in liquid form below 0 °C. Observations of SLW clouds have been carried out for several years at Dome C, the Concordia station (75° S, 123° E; 3233 m above mean sea level), combining observations from LIDAR, microwave radiometer and balloon-borne sondes. The present analysis is separated in two parts. Firstly, we will focus on the diurnal variation of the planetary boundary layer (PBL) from balloon-borne profile observations performed on January 23, 2023 establishing the presence of SLW clouds: 1) at the top of the PBL between the entrainment zone and the capping inversion layer, 2) higher up within a fossil layer, and 3) within the very cold stable boundary layer close to the surface as liquid fog. Secondly, from a statistical study covering several summer periods, we will show that SLW clouds are present from 400 to 600 m above ground level (agl) in the entrainment zone and within the stable boundary layer below 100 m agl where liquid fog can form, with temperatures from −25 °C to −35 °C and LWP (liquid water path, the vertically-integrated SLW content) less than 3.0 g m^{-2}.

1. Introduction

Clouds are one of the most important parameters to control the Earth's radiation balance, affecting the radiation reaching the surface and escaping to space, cooling or warming the atmosphere and supply water to the surface through precipitation (Tsushima et al., 2006; Komurcu et al., 2014; Storelvmo, 2017). The nature of the clouds (liquid and/or solid water) also affects the global radiative budget, thus the Earth climate evolution (Lemus et al., 1997; Choi et al., 2014; Lenaerts et al., 2017). In Antarctica, clouds are mainly composed of ice due to the very low average surface temperature below the freezing point of 0 °C (Lachlan-Cope, 2010). But, for more than ten years, satellite followed by airborne and ground-based observations have shown that a non-negligible fraction of the Antarctic clouds was constituted of liquid water (Grosvenor et al., 2012; Lachlan-Cope et al., 2016; Silber et al., 2019).

The term of supercooled liquid water (SLW) is generally employed when liquid water is present at temperature less than 0 °C. In theory, SLW can persist from 0 °C to −39 °C. Very little SLW is then expected because the ice crystals that form in this temperature range will grow at the expense of liquid droplets (called the "Wegener-Bergeron-Findeisen" process; Wegener, 1911; Bergeron, 1928; Findeisen, 1938; Storelvmo and Tan, 2015). Clouds containing SLW can also partly be made up of ice (solid water), and the term of mixed-phase cloud is thus employed. Because Antarctica is one of the driest and coldest place on Earth, the amount of water (liquid, solid and gaseous) is reduced compared with what is observed at tropical and middle latitudes. Nevertheless, the Antarctic clouds play a key role in the climate system by influencing the Earth's radiation balance, both directly at high southern latitudes and, indirectly, at the global level through complex teleconnections (Lubin et al., 1998).

Antarctic clouds show a fractional cloud cover ranging, on average, from 80 to 90 % near the coast to about 50–60 % near the South Pole (Bromwich et al., 2012; Listowski et al., 2019) with mixed-phase clouds preferably observed near the coast and ice clouds above the inner continent. As a consequence, SLW cloud fractions decrease sharply poleward, and are two to three times lower over the Eastern Antarctic Plateau than over the West Antarctica. Furthermore, the nature and

* Corresponding author.
E-mail addresses: philippe.ricaud@meteo.fr (P. Ricaud), pierre.durand@aero.obs-mip.fr (P. Durand), paolo.grigioni@enea.it (P. Grigioni), virginia.ciardini@enea.it (V. Ciardini), massimo.delguasta@ino.cnr.it (M. Del Guasta), giuseppe.camporeale@cnr.it (G. Camporeale), jean-luc.attie@aero.obs-mip.fr (J.-L. Attié), eric.bazile@meteo.fr (E. Bazile).

https://doi.org/10.1016/j.polar.2025.101256
Received 5 March 2025; Received in revised form 24 June 2025; Accepted 15 July 2025
Available online 16 July 2025

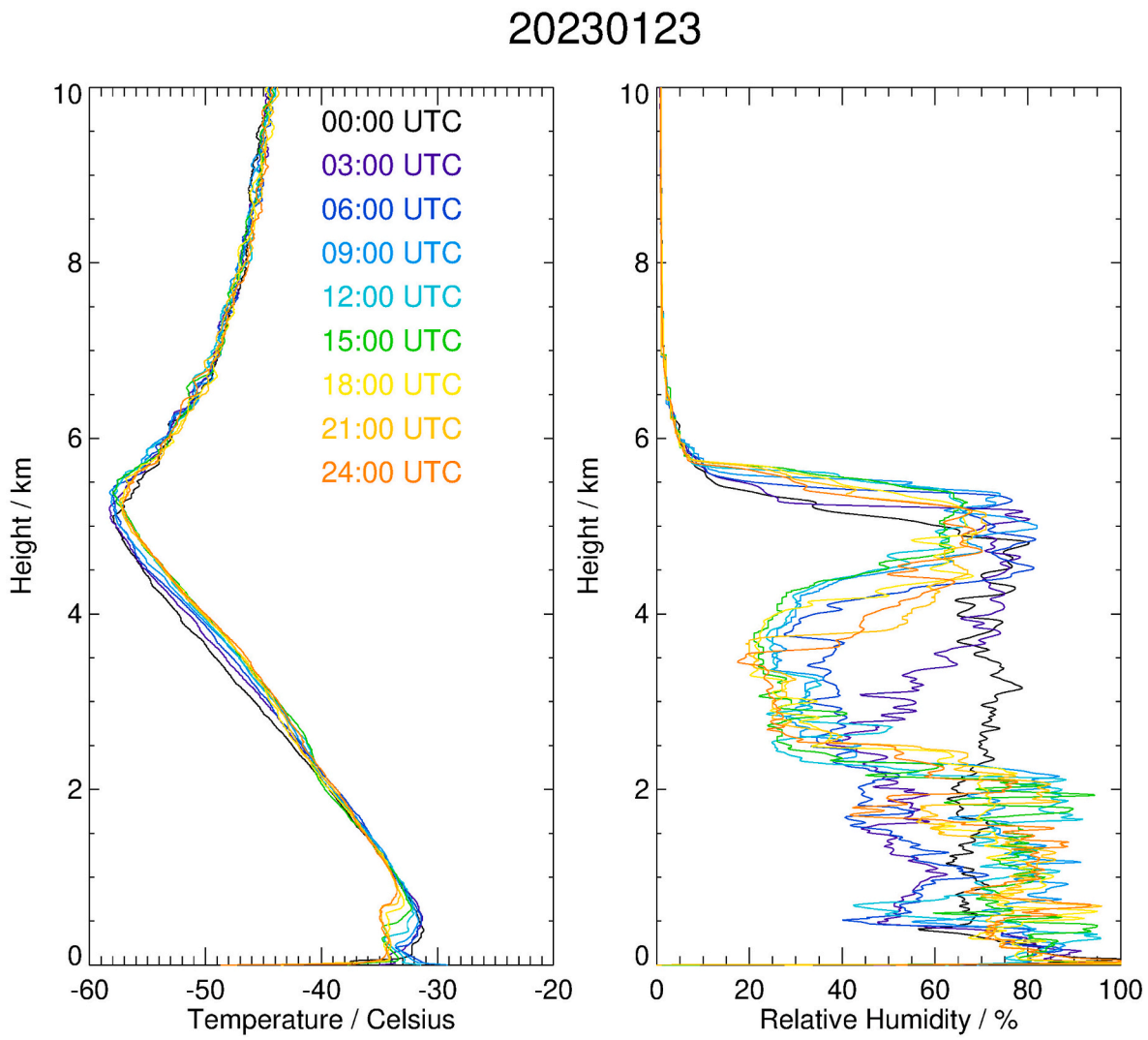

Fig. 1. Nine vertical profiles up to 10 km of (left) temperature (°C) and (right) relative humidity (%) observed every 3 h from January 23, 2023 at 00:00 UTC by means of PTU sondes.

optical properties of the Antarctic clouds depend on the type and concentration of cloud condensation nuclei and ice nucleating particles, and large uncertainties exist relative to their origin and abundance over Antarctica. But one important point remains that both research and operational weather prediction models inaccurately represent these clouds (and especially SLW clouds) in Antarctica (McCoy et al., 2015; Wang et al., 2022). As a consequence, simulations of net surface irradiance are biased by several tens W m^{-2} (Listowski et al., 2017; King et al., 2006, 2015; Bromwich et al., 2013) in and even beyond the Antarctic over the Southern Ocean (Lawson and Gettelman, 2014; Bodas-Salcedo et al., 2016; Young et al., 2019; Vignon et al., 2021).

From observations, climate models and meteorological reanalyses, it appears that, in Antarctica, the liquid water path (LWP), which is the vertically-integrated SLW content, is on average ranging 0–40 g m^{-2}, with slightly larger values in summer than in winter by 2–5 g m^{-2} (Lenaerts et al., 2017). On the Eastern Antarctic Plateau, LWP is less than 10 g m^{-2} in the CloudSat-Calipso satellite observations and is about 20–30 g m^{-2} in the CERES-EBAF satellite observations, namely 10–20 g m^{-2} less than in the Western Antarctica. At Dome C (Concordia station) in the Eastern Antarctic Plateau (75°06′ S, 123°21′ E, 3233 m above mean sea level, amsl), observations (Ricaud et al., 2024a; and b) show very low amounts of LWP (on average less than 10 g m^{-2}) consistent with meteorological analyses from ERA5 (Ricaud, 2025) and satellite observations (Lenaerts et al., 2017). On average, coastal LWP (including the Antarctic Peninsula) is 10–20 g m^{-2} greater than in the interior of the continent. In the Southern Ocean, LWP values range from 20 to 100 g m^{-2} in the CloudSat-Calipso observations and 80-50 g m^{-2} in the CERES-EBAF data (Lenaerts et al., 2017). In the Arctic Ocean (Lemus et al., 1997; Zhang et al., 2019; Lenaerts et al., 2017), satellite observations and CMIP5 model outputs show LWP values from 50 to 100 g m^{-2}, with much less values over Greenland (10–40 g m^{-2}). Finally, in the middle to tropical zones, LWP can reach 100–150 g m^{-2} (Lemus et al., 1997).

In Antarctica, since SLW contents are dramatically low, it is thus difficult 1) to observe SLW clouds, 2) to quantify the amount of liquid water present in the SLW clouds, and 3) to estimate the SLW cloud radiative forcing. Nevertheless, at Dome C (Concordia station), SLW clouds have been observed remotely and in situ, then analysed by combining observations with models. The presence of the SLW and mixed phase clouds over the station mainly diagnosed by a backscattered LIDAR has been investigated in Cossich et al. (2021). The precipitation nature has been classified into four types by Del Guasta et al. (2024): ice fogs, liquid fogs, mixed-phase clouds, and cirrus. The impact of SLW clouds on the net surface radiation has been studied in Ricaud et al. (2020) with simulations underestimating observations by 20–50 W m^{-2}. SLW clouds are preferably observed in summer with LWP

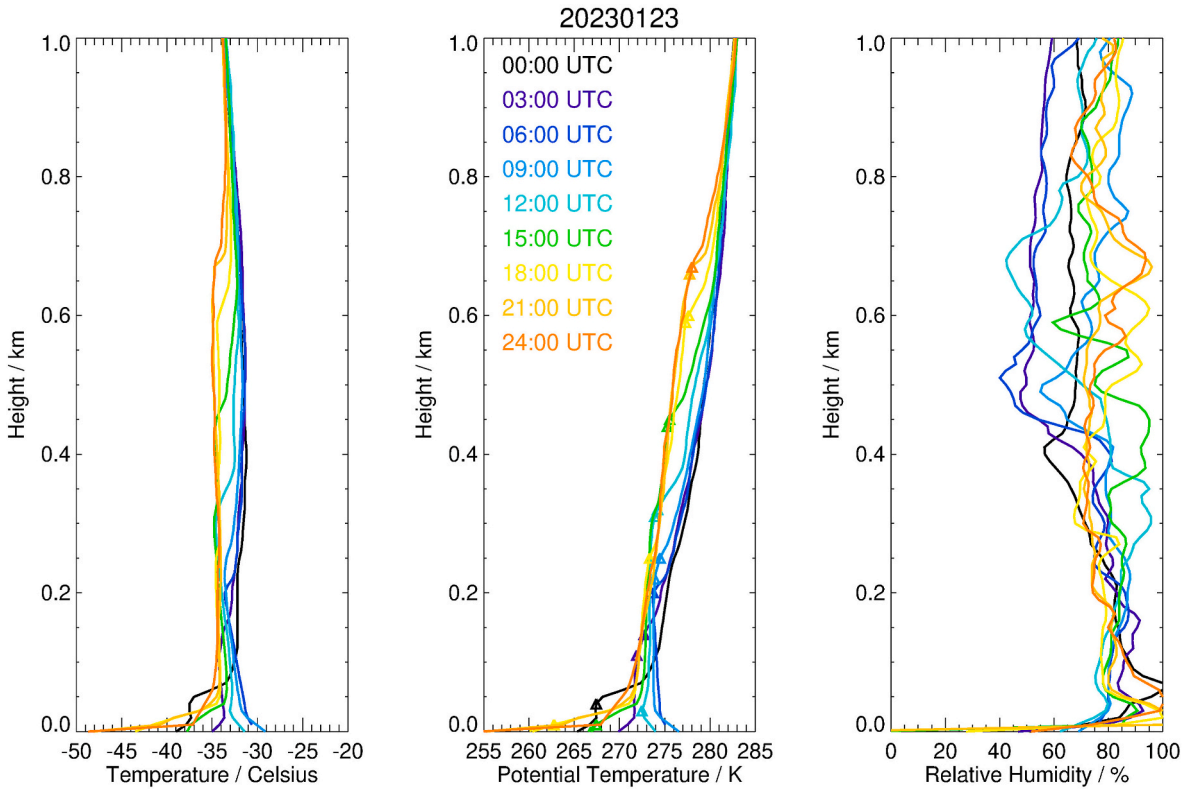

Fig. 2. Nine vertical profiles up to 1 km of (left) temperature (°C), (centre) potential temperature (K) and (right) relative humidity (%) observed every 3 h from January 23, 2023 at 00:00 UTC by means of PTU sondes. The heights of the inflection points in potential temperature profiles have been highlighted by triangles in the centre panel.

of a very small amount (<10 g m^{-2}), in-cloud temperatures ranging from −20 °C to −38 °C and a SLW cloud radiative forcing up to a maximum value of 40 W m^{-2} (Ricaud et al., 2024a).

In order to deepen the analyses performed so far, the present article aims at studying the diurnal evolution of SLW clouds observed over the Concordia station in summer and to attribute their cycle to the diurnal variation of the planetary boundary layer (PBL). To do so, we will mainly use observations performed on site by a series of different instruments over two different time frames: 1) a case study focussed on January 23, 2023 (from 00:00 to 24:00 UTC) and 2) a climatological study over four months of December (2018–2021). For the two time frames, we will take the advantage of continuous remote-sensing observations from: 1) the HAMSTRAD microwave radiometer providing the LWP and vertical distribution of temperature, 2) the backscatter, depolarization LIDAR providing the vertical distribution of SLW clouds and 3) a ceilometer providing the vertical distribution of clouds with no information on its nature. For the case study of January 23, 2023, we will complement these remote-sensing observations by in-situ observations of temperature and relative humidity from meteorological sondes attached to balloons launched every 3 h from 00:00 to 24:00 UTC. Finally, we will evaluate the ability of the ARPEGE numerical weather prediction (NWP) model from Météo-France and the ERA5 reanalyses from the European Centre for Medium-Range Weather Forecasts (ECMWF) to estimate the presence of SLW clouds on that particular day.

The article is structured as follows. Section 2 will present the different data sets. Section 3 will focus on the analysis of the case study (January 23, 2023) while section 4 will enlarge the study to the climatological analysis (four months of December 2018–2021). Conclusions will be drawn in section 5.

2. Data sets

2.1. PTU meteorological radiosondes

We used PTU sondes of the Vaisala RS-41 SGP type (an upgraded version of the Vaisala's RS92 radiosonde), which are now also used operationally at the Concordia station to obtain wind, temperature and humidity vertical profiles every day at 12:00 UTC.

2.2. LIDAR

The tropospheric depolarization LIDAR (532 nm) has been operating at Dome C since 2008 (see http://lidarmax.altervista.org/lidar/Antarctic%20LIDAR.php). The LIDAR provides 5-min tropospheric profiles of aerosols and clouds continuously, from 20 to 7000 m above ground level (agl), with a resolution of 7.5 m. LIDAR depolarization (Mishchenko et al., 2000) is a robust indicator of non-spherical shape for randomly oriented cloud particles. A depolarization ratio below 10 % is characteristic of SLW droplets, while higher values are produced by ice particles. The possible ambiguity between SLW droplets and oriented ice plates is avoided at Dome C by operating the LIDAR 4° off-zenith (Hogan and Illingworth, 2003).

2.3. HAMSTRAD

HAMSTRAD is a microwave radiometer that profiles water vapour and tropospheric temperature together with liquid water path (LWP) above Dome C. Measuring at both 60 GHz (oxygen molecule line (O_2) to deduce the temperature) and 183 GHz (H_2O line), this unique radiometer was installed on site for the first time in January 2009 (Ricaud et al., 2010) and is automatically observing since then. The measurements of the HAMSTRAD radiometer allow the retrieval of the vertical profiles of water vapour and temperature from the ground to 10-km altitude. In the

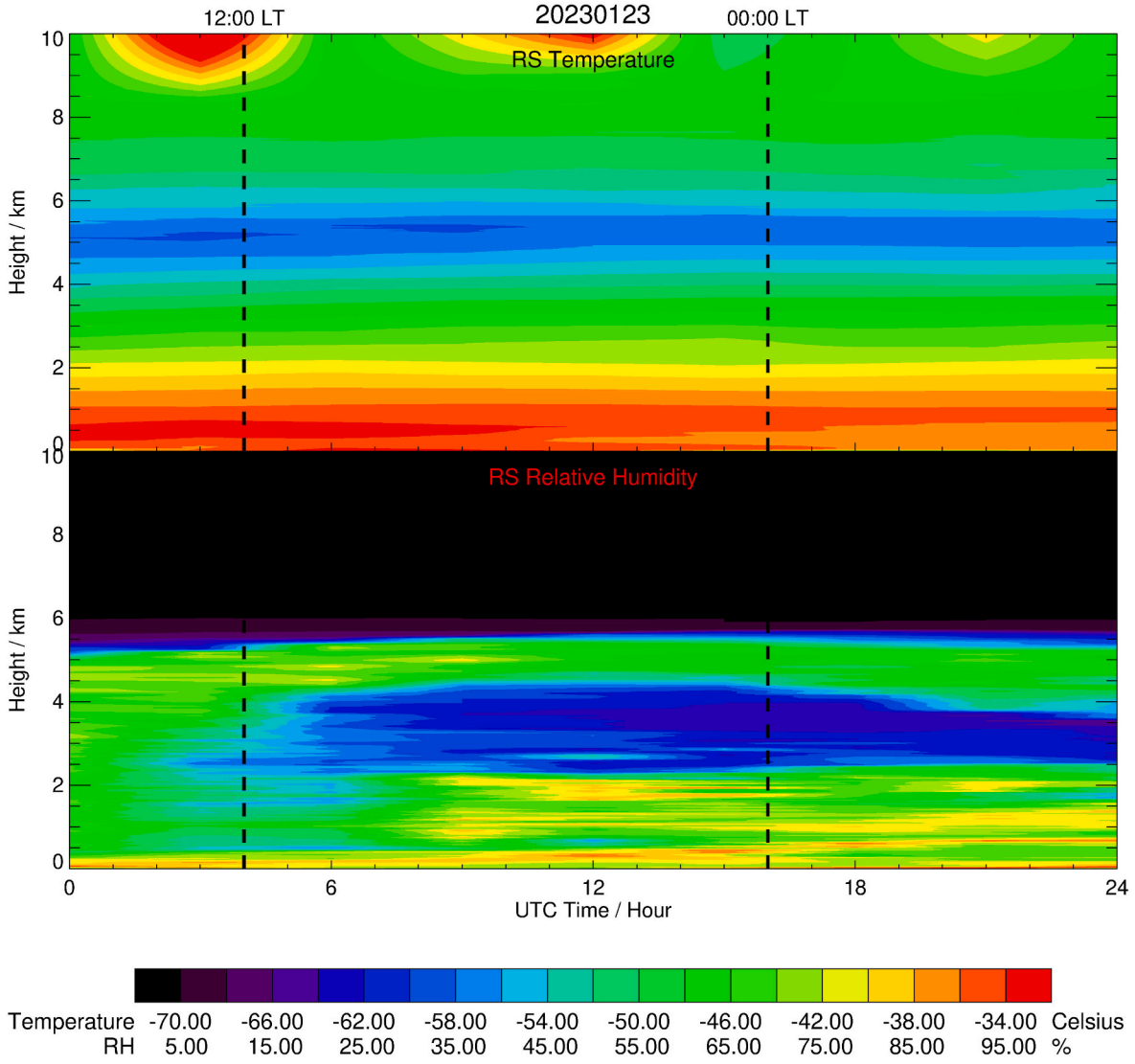

Fig. 3. Diurnal variation of (top) temperature and (bottom) relative humidity (RH) profiles observed on January 23, 2023 by means of PTU sondes.

0 to 1600-m altitude range selected for the present analysis of temperature measurements, the vertical levels of the retrieval are: 0, 10, 30, 50, 75, 100, 125, 150, 200, 250, 325, 400, 475, 550, 625, 700, 800, 900, 1000, 1150, 1300, 1450, and 1600 m. The time resolution is adjustable and fixed at 60 s since 2018. The temporal resolution on the instrument allows for the analysis of various atmospheric processes including e.g. the diurnal evolution of the PBL (Ricaud et al., 2012) and the presence of clouds and diamond dust (Ricaud et al., 2017) together with SLW clouds (Ricaud et al., 2020, 2024a) through the measurement of the LWP (g m^{-2}).

2.4. Ceilometer

In our study, we have also used the CL51 Vaisala ceilometer (https://www.vaisala.com) that measures cloud height and precipitation at the Concordia station since 2022 (https://www.climantartide.it/). It employs a pulsed diode laser LIDAR technology operating at 910 ± 10 nm where short, powerful laser pulses are sent out in a vertical or near-vertical direction. The light backscatter – caused by haze, fog, mist, virga, precipitation and clouds – is measured as the laser pulses traverse the sky. The main difference with the aerosol LIDAR described in section 2.2 is that it cannot distinguish between in-cloud liquid and solid phase because it does not measure depolarization ratio. The ceilometer observations were nevertheless used to check the consistency with the clouds and precipitations observed by the LIDAR on January 23, 2023 at the Concordia station.

2.5. ARPEGE

In this study, the global model ARPEGE, designed for NWP (Pailleux et al., 2015), is run with its finest horizontal resolution centred over Dome C (instead of over France as in its operational mode). A 4D variational (4DVar) assimilation was performed every 6 h. The meteorological analyses were given by the ARPEGE-SH system together with the 24-h forecasts at the node the closest to the location of Dome C. Two analyses at 00:00 and 12:00 UTC were represented in the present study together with hourly forecasts. The horizontal resolution was 7.5 km at Dome C. The vertical resolution was constituted by 22 levels below 1000 m and 28 levels below 1500 m agl. The time resolution was set to 1 h. Several ARPEGE output parameters were selected for analysis: cloud fraction, ice and liquid water mixing ratios, PBL height, relative humidity and temperature. The diurnal variation of the top of the PBL is calculated by ARPEGE as the level where the turbulence kinetic energy becomes lower than 0.01 m^2 s^{-2}. Consistent with Ricaud et al. (2020), we have modified the ice/liquid partition function for temperatures below 0 °C in order to obtain more realistic SLW contents for

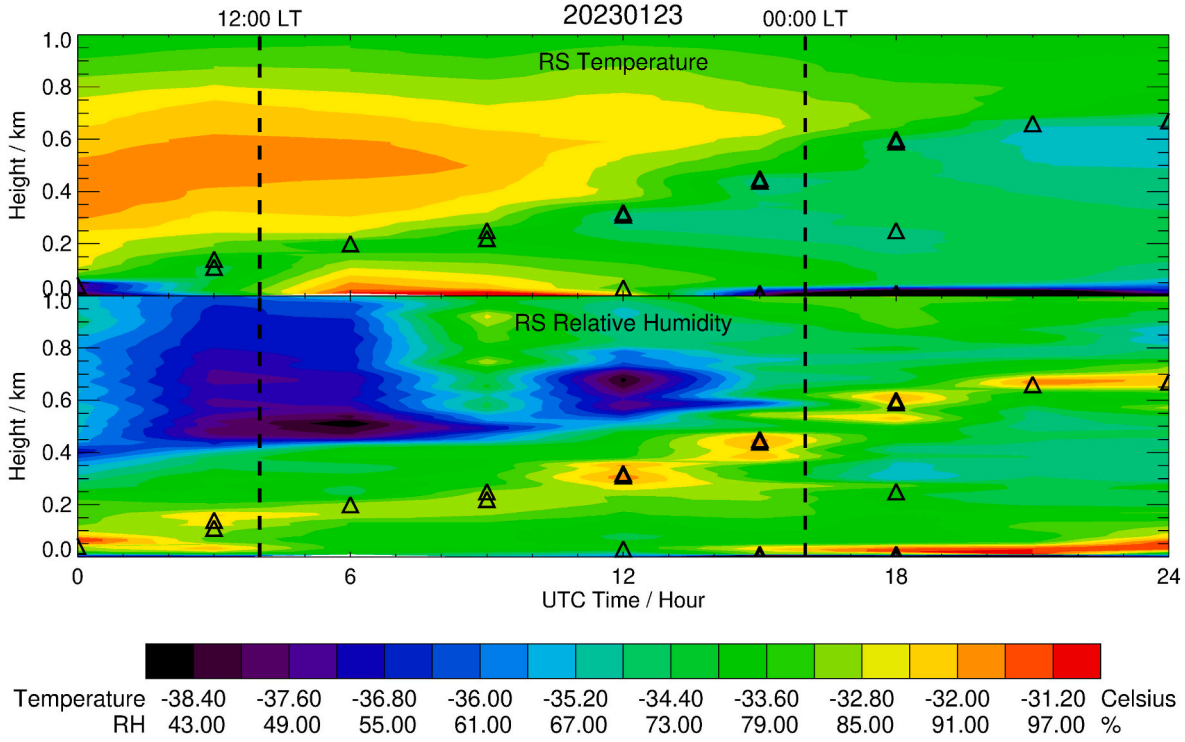

Fig. 4. Same as Fig. 3 but from 0 to 1 km. The heights of the inflection points in potential temperature profiles have been highlighted by triangles for each profile measured every 3 h.

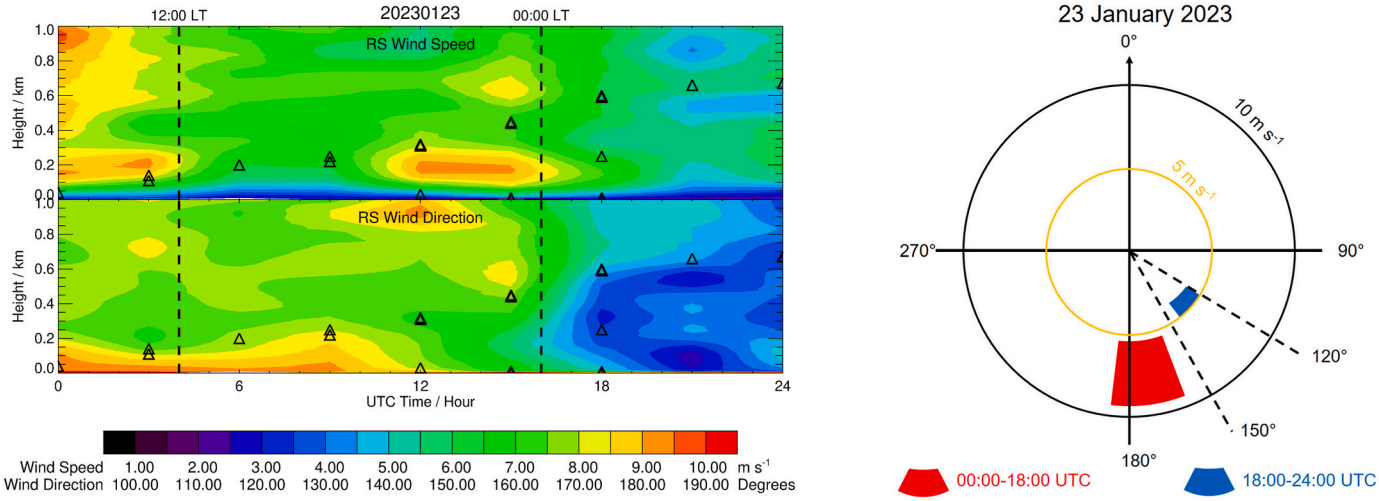

Fig. 5. (Left) Diurnal variation of (top) wind speed and (bottom) wind direction observed on January 23, 2023 by means of PTU sondes from 0 to 1 km. Note that the heights of the inflection points in potential temperature profiles have been highlighted by triangles for each profile measured every 3 h (Right) Simplified wind rose (wind speed and direction) representing the two regimes identified on January 23, 2023: before (red) and after (blue) 18:00 UTC. (For interpretation of the references to colour in this figure legend, the reader is referred to the Web version of this article.)

temperatures between −20 °C and −40 °C.

2.6. ERA5

In this analysis, we exploit a state-of-the-art reanalysis dataset provided by the ECMWF and known as ECMWF Reanalysis v5 (ERA5). ERA5 (Hersbach et al., 2020) is the fifth generation ECMWF global atmospheric reanalysis covering the period from January 1940 to the present day with meteorological parameters (near-surface air temperature and wind) validated over West Antarctica (Tetzner et al., 2019). We want to confront the calculated clouds (ice and SLW) with the observations performed at the Concordia station on January 23, 2023. The scheme implemented with distinct liquid- and ice-water prognostic variables and parameterized depositional growth allows SLW to exist at all temperatures between 0 °C and the homogeneous freezing threshold temperature defined at −38 °C (Forbes and Ahlgrimm, 2014). The pressure levels are every 50 hPa from 650 to 300 hPa. This corresponds to only three levels below 1.5 km agl at approximately 0, 530 and 1150 m agl. The outputs are given at an hourly rate from 00:00 to 24:00 UTC.

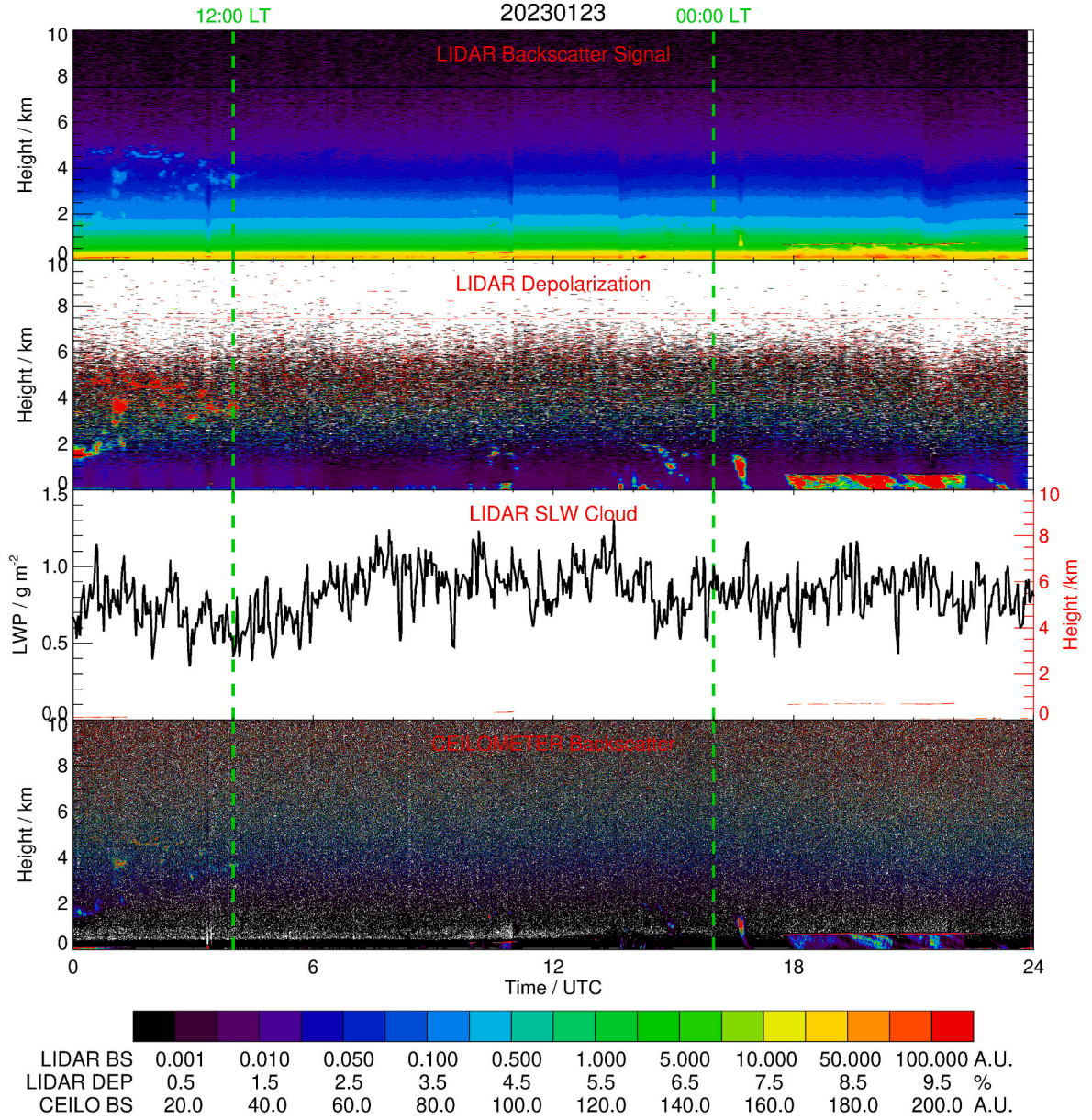

Fig. 6. (From top to bottom) Diurnal variation of the LIDAR backscatter signal (LIDAR BS, arbitrary unit) and depolarization ratio (LIDAR DEP, %), the LWP (g m^{-2}) from HAMSTRAD superimposed with the SLW cloud thickness (red area) derived from the LIDAR observations (red y axis on the right) and the ceilometer backscatter signal (CEILO BS, arbitrary unit) observed on January 23, 2023 from 0 to 10 km agl. Two dashed green vertical lines indicate 12:00 and 00:00 LT. (For interpretation of the references to colour in this figure legend, the reader is referred to the Web version of this article.)

2.7. Periods of study

We have separated our analysis following two approaches. The first one consists in a case study based on the analysis of temperature and relative humidity profiles measured by meteorological radiosondes every 3 h from 00:00 to 24:00 UTC. These observations are coupled with remote-sensing measurements from HAMSTRAD and the LIDAR to deduce the diurnal behaviour of SLW clouds as a function of the PBL top height. The second approach is based on the climatological data set combining HAMSTRAD and LIDAR observations of SLW clouds obtained over four months of December (2018–2021) and intensively analysed in Ricaud et al. (2024a). We will check whether the diurnal variation of the PBL top height impacting the formation of SLW clouds from the case study is widely valid in a climatological approach.

3. Diurnal variation of the PBL: case study

3.1. In-situ observations

At the Concordia station, there are 8 h difference between the local time (LT) and coordinated universal time (UTC) with LT = UTC + 8 h. On January 23, 2023, nine PTU sondes were launched using a standard meteorological balloon every 3 h from 00:00 to 24:00 UTC. Note that at 12:00 UTC, we have used the observations performed by the operational launch performed once every day. The vertical distributions of temperature (T, °C) and relative humidity (U, %) from the ground to either 10 km agl or 1 km agl are shown in Figs. 1 and 2, respectively. We have also represented the vertical distribution of the potential temperature (θ, K) calculated as:

$$\theta = T(P_0/P)^{R/C_p} \quad (1)$$

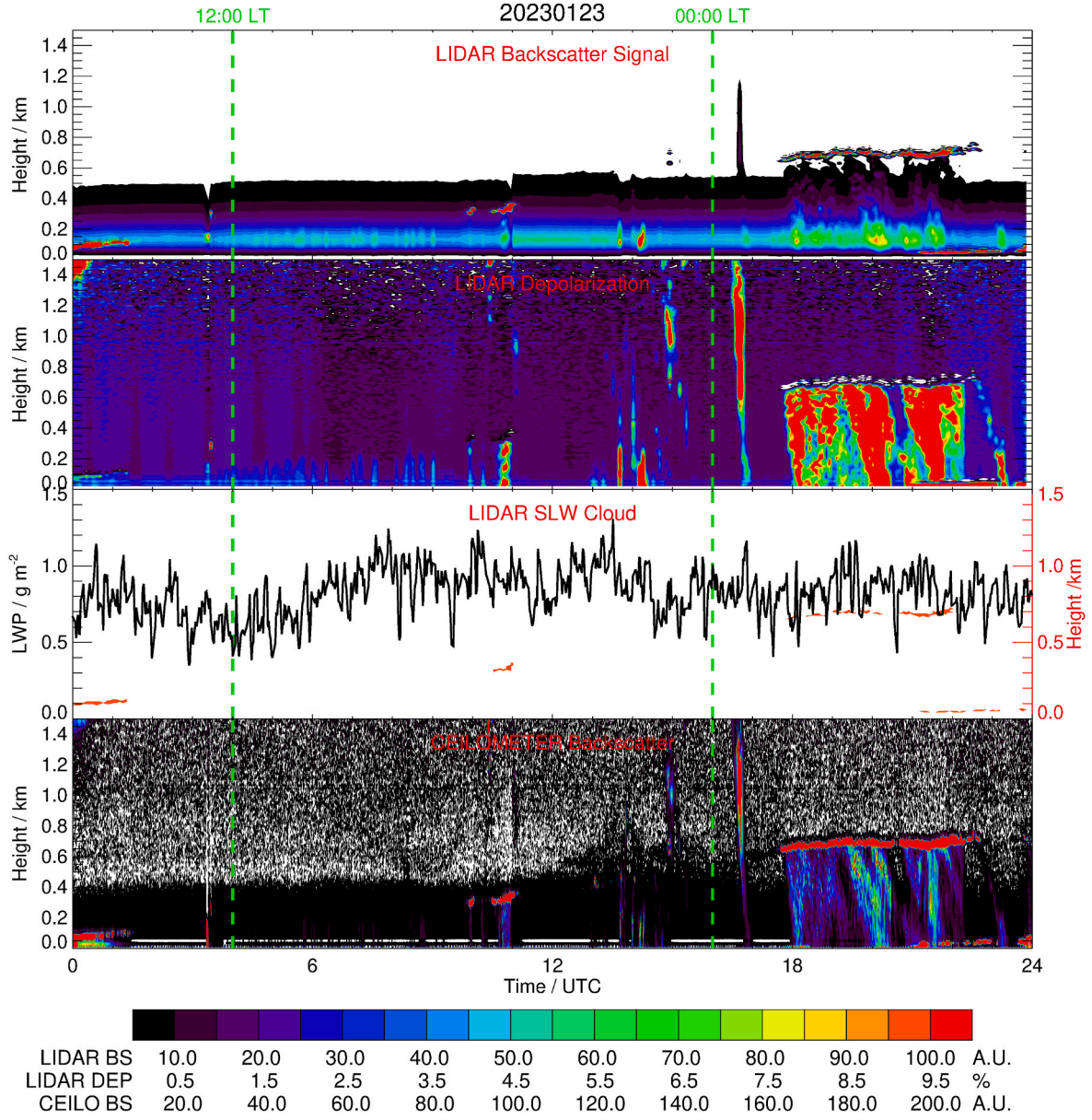

Fig. 7. Same as Fig. 6 but below 1.5 km.

where T is the temperature (K), P the pressure (hPa), P_0 the reference pressure (1000 hPa), R the gas constant of dry air (J kg^{-1} K^{-1}) and C_p the heat capacity at constant pressure (J kg^{-1} K^{-1}). R/C_p is taken at 0.286. We have characterized inflection points heights $H(\theta_{inf})$ in the potential temperature vertical profiles when the second derivatives in θ with respect to the height z ($d^2\theta/dz^2$) are greater than an empirical threshold value typically set to 8.2 10^{-4} K m^{-2}. From now, we will always refer to heights agl.

The diurnal cycle in T and U shows a large variability of ±3 °C and 20–95 % in the free troposphere below about 6 km, and even larger in the lowermost troposphere below 1 km, reaching ±10 °C and 0–100 %, respectively. The profile of the potential temperature below 1 km also shows this large amplitude of the diurnal cycle with the heights of the inflection points varying from ~50 to ~700 m. Within a thin layer below the level of the inflection point in θ, clouds may remain whatever their phase (solid, supercooled liquid or mixed) if the atmosphere is cold enough and reaches saturation ($U \geq 95$ %). This level is also a good tracer of the PBL top height. Therefore, for this particular day, we can anticipate that the PBL top height was varying between ~50 and ~700 m over 24 h.

In Fig. 3, we present the time-height cross-section over 24 h of T and U observed by the sondes below 10 km. If we consider the tropospheric layer below ~6 km, we clearly see a temperature variability of about 5 °C within the 4–6 km layer and below 1 km. For U, a large variability is observed below 6 km from 20 to 100 %. If we now consider in more detail the lowermost layer below 1 km (Fig. 4), the layer below 100 m shows a classical diurnal temperature evolution, with temperature greater by ~8 °C from 04:00 UTC (12:00 LT) to 14:00 UTC (22:00 LT) than in the remaining periods. Within the layer 400–600 m, the atmosphere is continuously cooling from −32 to −36 °C. Note that SLW clouds can remain below 0 °C down to −38 °C. As expected, the diurnal variation of U below 100 m presents high values after local midnight and a drying after local noon. Above 100 m, there is a high U (85–100 %) tongue over the 24 h starting at ~100 m at 00:00 UTC and rising progressively to reach ~700 m at 24:00 UTC. From 200 m above this tongue, the atmosphere is very dry (<35 %) from 00:00 to 16:00 UTC. We have superimposed the heights of the inflection points in θ as calculated from the profiles observed every 3 h. It is very interesting to

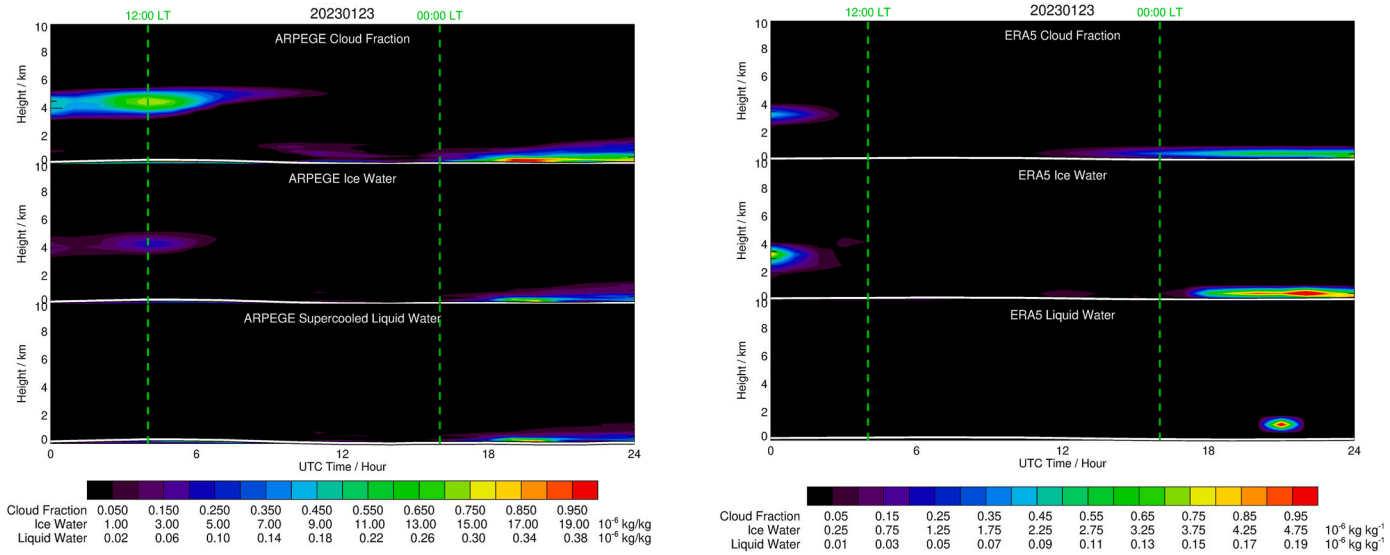

Fig. 8. (From top to bottom): Diurnal variation of the cloud fraction, ice water and SLW content calculated by (left) ARPEGE and (right) ERA5 on January 23, 2023 from 0 to 10 km. Two dashed green vertical lines indicate 12:00 and 00:00 LT. (For interpretation of the references to colour in this figure legend, the reader is referred to the Web version of this article.)

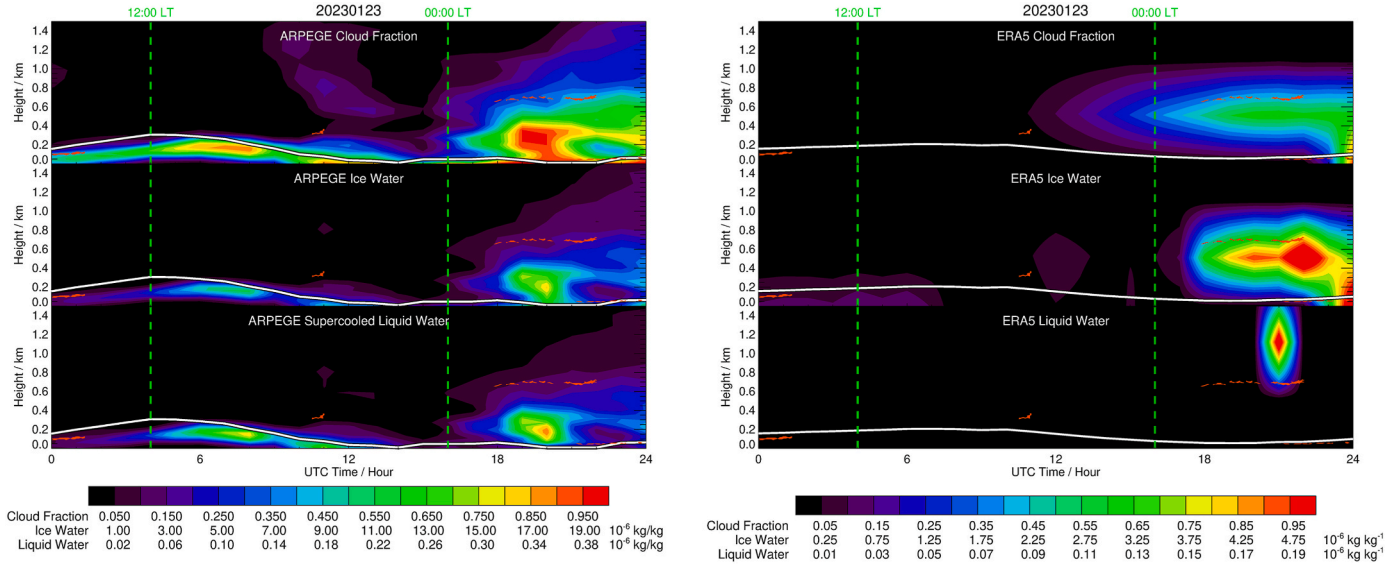

Fig. 9. Same as Fig. 8 but from 0 to 1.5 km. The SLW cloud thickness (red area as in Fig. 6 and 7) derived from the LIDAR observations and the PBL top height (white line) calculated by (left) ARPEGE and (right) ERA5 have been superimposed on all the panels. Note that the colour tables are different for ARPEGE and ERA5 panels. (For interpretation of the references to colour in this figure legend, the reader is referred to the Web version of this article.)

note that, over the whole day, the height of the inflection point follows the tongue of humid and cold layer from ~100 to ~700 m. In other word, this tongue is a good candidate to support the presence of clouds and, given the in-tongue temperature above −38 °C, the presence of SLW clouds.

The wind speed (m s^{-1}) and direction (°) as measured by the PTU sondes over the day are presented in Fig. 5 from the ground to 1 km. If we except the 50-m layer just above the ground, the wind speed shows two regimes: 1) before 18:00 UTC with speed ranging from 6.0 to 9.0 m s^{-1} and 2) after 18:00 UTC with speed reduced to 4.0–5.0 m s^{-1}. The wind orientation from 0 to 1 km is different in these 2 regimes with an orientation ranging from 160° to 185° before 16:00–18:00 UTC and from 120° to 140° after 18:00 UTC. Note that an orientation of 0° means that the wind is blowing southward and an orientation of 90° means that the wind is blowing westward.

3.2. *Remote-sensing observations*

In this section, we analyse the observations of clouds performed by the LIDAR and the ceilometer together with the LWP measured by the HAMSTRAD radiometer on January 23, 2023. In Fig. 6, we present the LIDAR backscatter signal and depolarization ratio, the LWP, and the ceilometer backscatter signal from the ground to 10 km. As discussed in Ricaud et al. (2024a), we consider that an SLW cloud is detected when the depolarization ratio is less than 5 %. Furthermore, we have superimposed the presence of SLW clouds on the LWP panel. Fig. 7 is as Fig. 6 but from the ground to 1.5 km.

Above 2 km (Fig. 6), the LIDAR and, to a lesser extent, the ceilometer observe ice clouds (depolarization ratio greater than 10 %) between 3 and 5 km from 00:00 to 04:00 UTC. These are obviously cirrus clouds.

Below 1.5 km (Fig. 7), the LIDAR and the ceilometer show very thin

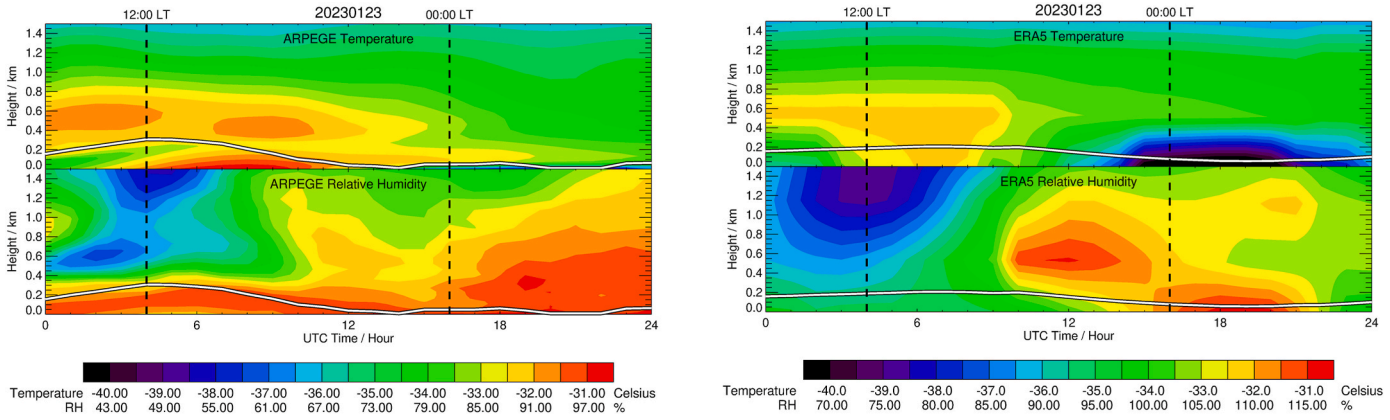

Fig. 10. Diurnal variation of (top) temperature and (bottom) relative humidity (RH) calculated by (left) ARPEGE and (right) ERA5 on January 23, 2023 below 1.5 km, with the calculated PBL top height represented by a white thick line. Two dashed green vertical lines indicate 12:00 and 00:00 LT. Note that the RH colour scales are different for the ARPEGE and ERA5 panels. (For interpretation of the references to colour in this figure legend, the reader is referred to the Web version of this article.)

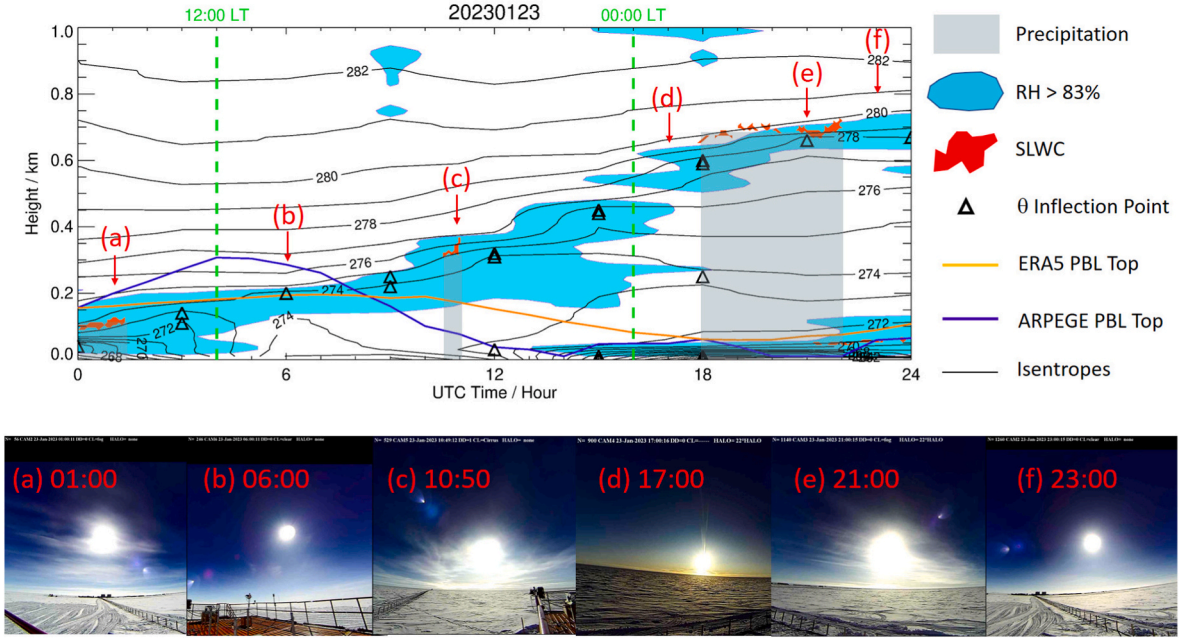

Fig. 11. (Top) Diurnal variation below 1 km of height ranges with relative humidity greater than 83 % (light blue areas), potential temperature (isolines), SLW clouds (red areas) and inflection points in the potential temperature profiles (triangles) observed on January 23, 2023 from the PTU sondes, together with the top of the PBL diagnosed from the ARPEGE simulations (thick purple line) and the ERA5 reanalyses (thick orange line). Periods with observed precipitation at the ground are greyed out. Two dashed green vertical lines indicate 12:00 and 00:00 LT. (Bottom) Six webcam images showing the cloud coverage at: a) 01:00 UTC, b) 06:00 UTC, c) 10:50 UTC, d) 17:00 UTC, e) 21:00 UTC and f) 23:00 UTC. (For interpretation of the references to colour in this figure legend, the reader is referred to the Web version of this article.)

(10–30 m deep) SLW clouds (depolarization ratio less than 5 %) over four periods and heights: 1) 00:00–01:30 UTC around 50 m, 2) 10:30–11:00 UTC around 300 m, 3) 18:00–22:00 UTC around 700 m, and 4) 22:00–24:00 UTC around 30 m. The observed SLW clouds are so thin that the LWP measured by HAMSTRAD does not exhibit any significant change over 24 h (0.5–1.0 g m^{-2}) when the SLW clouds are present. It has already been noted (Ricaud et al., 2024b) that the microwave radiometer, due to its viewing geometry, is sensitive to overcast clouds. We will show later (section 3.4) that the meteorological situation on that day was highlighting only scattered clouds, to which HAMSTRAD is quite insensitive regarding LWP measurements. Several points need to be highlighted. 1) Associated with the presence of the SLW clouds is ice precipitation down to the ground forming vertical stripes in Figs. 6 and 7. 2) Ice clouds are also detected slightly above the SLW clouds. In that case, we can label these clouds as mixed-phase clouds. And 3) the ceilometer can detect clouds consistent with the LIDAR observations but cannot attribute the water phase.

3.3. Model results

We can now verify whether NWP models succeed in providing SLW clouds in their calculations. For ARPEGE, we have modified the ice/liquid partition function to favour SLW below 0 °C at the expense of ice, consistent with the method presented in Ricaud et al. (2020). For both ARPEGE and ERA5, we present the time evolution on January 23, 2023 of the cloud fraction, as well as ice and liquid water contents below 10 and 1.5 km in Figs. 8 and 9, respectively.

Cirrus clouds are diagnosed by ARPEGE around 4.0 km from 00:00 to

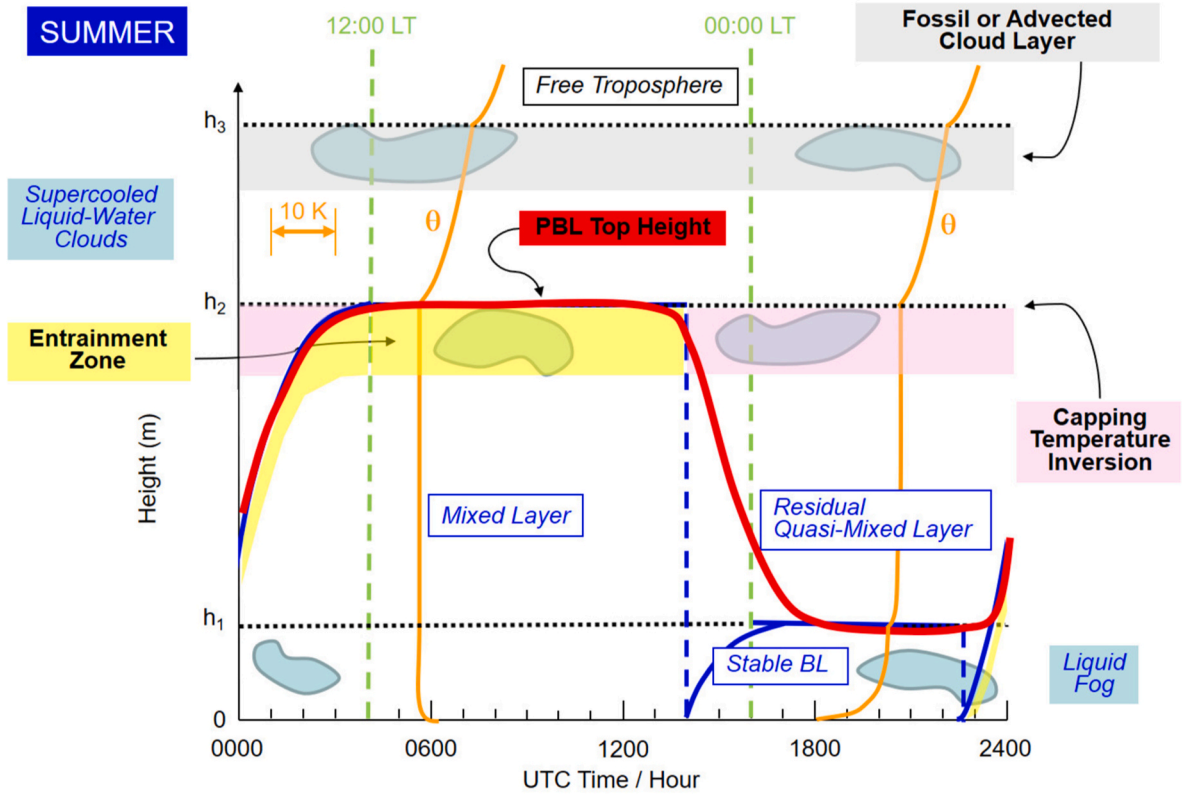

Fig. 12. Figure modified and updated from Fig. 18 of Ricaud et al. (2020) showing the diurnal evolution of the different layers in the PBL with h_1 the top of the stable layer, h_2 the daily overall top of the mixed layer and h_3 the top of the fossil layer. The orange lines symbolize the vertical profiles of potential temperature θ, and the light blue areas the SLW clouds or liquid fog in the stable boundary layer. The yellow area represents the "entrainment zone" at the upper part of the (cloudy or cloud-free) mixed layer topped by the "capping temperature inversion". The pink area is the remnant of the entrainment zone once it is decoupled from the surface. The upper part of the fossil layer is represented by a grey area and can be seen as a remnant of the entrainment zone created one or a few days before above the station or as a cloud layer advected by long-range transport. The diurnal variation of the top of the PBL is represented by a thick red line. Note that LT = UTC +8 h, midnight and noon in the local time reference being indicated by the green dashed lines. (For interpretation of the references to colour in this figure legend, the reader is referred to the Web version of this article.)

10:00 UTC, whereas ERA5 places them around 3.0 km between 00:00 and 03:00 UTC. This is more or less consistent with the LIDAR observations (Fig. 6) at 4.0 km from 00:00 to 04:00 UTC. In the lower layers (Fig. 9), mixed-phase clouds are calculated by ARPEGE from 00:00 to 14:00 UTC below the top of the PBL (0–300 m) and from 16:00 to 24:00 UTC above the top of the PBL (100–600 m). In ERA5 from 00:00 to 07:00 UTC, clouds are essentially below the PBL top (0–100 m) and constituted of ice, whereas from 16:00 to 22:00 ice crystals lie above the PBL top (200–800 m) and a single liquid water cloud appears at 22:00 UTC at 1.2 km. After 22:00 UTC, ERA5 is also able to simulate an ice cloud below 200 m. To summarize, ARPEGE was able to simulate mixed-phase clouds in the first part of the day while ERA5 was not, and in the second part of the day, ARPEGE simulated SLW clouds 400 m below the observations and ERA5 400 m above the observations. The slimness of the observed SLW clouds (<100 m) was reproduced neither by ARPEGE (200–400 m) nor by ERA5 (~800 m). This is essentially due to the vertical resolution of the NWPs below 1500 m: from 20 to 120 m for ARPEGE and ~500 m for ERA5.

For both ARPEGE and ERA5, we present the temperature and relative humidity time evolution from the ground to 10 and 1.5 km in Fig. 10. Below 100 m, the amplitude of the diurnal cycle in temperature is around 10 °C that is consistent with observations from the radiosondes, but ARPEGE shows a warm bias of about 5 °C compared to both observations and ERA5. Regarding the relative humidity, ERA5 is much wetter than ARPEGE by 20–30 % exhibiting a supersaturation of ~110 % around 18:00 UTC (note that the colour tables are different for the ARPEGE and ERA5 RH panels), and ARPEGE is on average 10 % wetter than the radiosondes. Note that the diurnal variation of the PBL top height is consistent between ARPEGE and ERA5 showing a maximum of ~300 m around 05:00 UTC in ARPEGE and of ~200 m at 06:00–10:00 UTC in ERA5 and a minimum of ~30 m around 13:00–14:00 and 20:00–22:00 UTC in ARPEGE and of ~50 m around 18:00–20:00 UTC in ERA5.

3.4. Synthesis of the case study

We can synthetize our findings based on our case study following Fig. 11. We have highlighted the diurnal variation of: 1) the potential temperature from the sondes, 2) the RH greater than 83 % from the sondes, 3) the observed SLW clouds from the LIDAR, 4) the inflection points in θ profiles from the sondes, 5) the precipitation from the LIDAR and 6) the PBL top height as calculated by ARPEGE and ERA5. We have selected six different times when SLW clouds are or are not observed, based on the webcam images recorded automatically by a device installed on the roof of the so-called Physics shelter where HAMSTRAD and the LIDAR are set up. They are a) 01:00 UTC (scattered SLW clouds), b) 06:00 UTC (clear sky), c) 10:50 UTC (scattered SLW clouds), d) 17:00 UTC (clear sky), e) 21:00 UTC (scattered SLW clouds) and f) 23:00 UTC (clear sky).

The SLW clouds are always located within a wet layer (U > 83 %) either close to the surface (liquid fog below 50 m) or higher up in a domain encompassing an inflection point in θ profile. The SLW clouds as deduced from the LIDAR depolarization ratios less than 5 % are consistent with the webcam images. From 00:00 to 12:00 UTC, the height of the inflection point moves from 100 to 250 m following the 274-K isentrope. This clearly indicates the top of the PBL. After 12:00

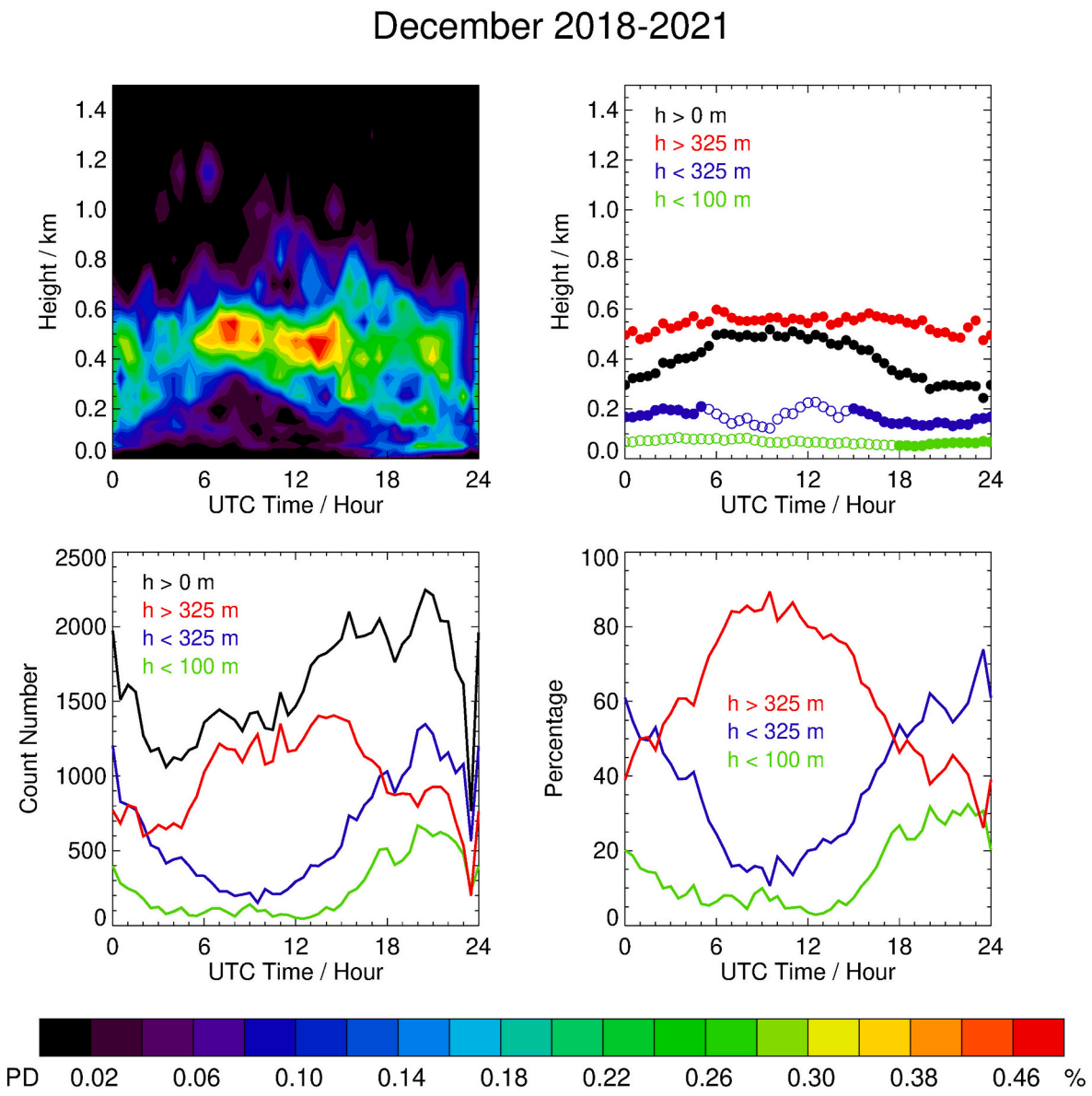

Fig. 13. (Top Left) Probability density (PD, %, see text for definition) of the height of the SLW clouds (km) as a function of UTC Time (Hour) in December 2018–2021. (Top Right) Mean height of SLW clouds as a function of UTC Time (Hour) in December 2018–2021 considering: all the SLW clouds (h > 0 m, black), SLW clouds above 325 m (red), below 325 m (blue), and below 100 m (green). (Bottom Left) Number of SLW clouds as a function of UTC Time (Hour) in December 2018–2021 considering: all the SLW clouds (h > 0 m, black), SLW clouds above 325 m (red), below 325 m (blue), and below 100 m (green). (Bottom Right) Percentage of the height range at which SLW clouds occur as a function of UTC Time (Hour) in December 2018–2021 considering: SLW clouds above 325 m (red), below 325 m (blue), and below 100 m (green). In the top right Figure, we have visualized the mean height as a filled or open circle when the percentage is greater or less than 25 %, respectively. (For interpretation of the references to colour in this figure legend, the reader is referred to the Web version of this article.)

UTC, three regimes are observed. 1) An inflection point very close to the surface (<30 m) where liquid fog can develop in a very cold and wet environment. 2) An inflection point at 18:00 UTC (with a θ value of 274 K) that is a remnant of the PBL present before 12:00 UTC above the station. And 3) an inflection point around 277 K that cannot be directly related with the PBL developing this day at the Concordia station but can be seen either as a fossil layer formed days before at the Concordia station or as a cloud layer advected by long-range transport. In that case, it is thus possible to observe at the same time (e.g. 18:00 UTC) up to three inflection points as a signature of three different regimes.

Based on this case study, we can then propose a schematic evolution of the PBL that affects the presence of SLW clouds (Fig. 12) initially based on Stull (2012) and adapted to the Antarctic polar atmosphere in Ricaud et al. (2020). From around 00:00 UTC (08:00 LT), the surface warms up and a mixed layer is formed that progressively thickens. In the upper part, an entrainment zone develops, with high values of relative humidity, location of the SLW clouds. After 12:00 UTC (20:00 LT), the surface cools down, a stable boundary layer develops close to the surface where a liquid fog can occur if U is high enough. Above, there remains a residual quasi-mixed layer, which is no longer connected to the surface, but in the upper part, named as capping temperature inversion, SLW clouds still may be present. The diurnal variation of the PBL top height follows the top of the entrainment zone during the warm period and the top of the stable boundary layer during the cold period. In addition to these two phenomena, a fossil layer that can be seen as a remnant of the entrainment zone created one or more days before above the station or a cloud layer advected through long-range transport can superimpose above the PBL top height and show SLW clouds.

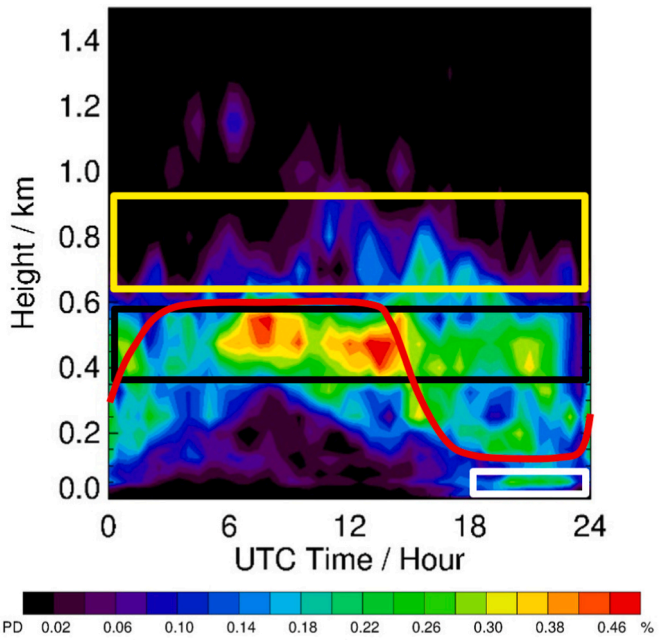

Fig. 14. Height of the SLW clouds (same as the upper left panel on Fig. 13), on which have been superimposed the PBL top height (as defined in Fig. 12, red line), the (active or residual) entrainment zone where SLW clouds form and may remain (black rectangle), the fossil or advected cloud layer where SLW clouds may still be present (yellow rectangle) and the stable boundary layer (white rectangle) where liquid fog may form. (For interpretation of the references to colour in this figure legend, the reader is referred to the Web version of this article.)

4. Diurnal variation of SLW clouds: climatology

4.1. Methodology

In this section, we want to confront our findings issued from a case study to a climatological analysis of SLW clouds observations performed during the month of December 2018, 2019, 2020 and 2021 and presented in Ricaud et al. (2024a). We show the diurnal distributions of SLW clouds (as detected by the depolarization ratio) as a function of: a) the height h, b) the in-cloud temperature T and c) the LWP, and check whether they are consistent with the general view of the PBL diurnal evolution shown in Fig. 12.

The 2D probability density (PD) is calculated for paired binned datasets and defined as $PD_{ij} = 100\ \frac{N_{ij}}{N_t}$, where N_{ij} and N_t are the count number in the bin ij and the total count number ($N_t = \sum_{j=1}^{L}\sum_{i=1}^{M} N_{ij}$), respectively, with M and L being the total number of bins in time t (counted from 00:00 to 24:00 UTC, in 0.5 h-wide intervals whatever the date, for the whole data set), and either in h, T or LWP, respectively. The h_j bins match the heights of the radiometer vertical grid, to which are associated the temperature retrieval T_j at the same height intervals. For a given height, the temperature values are binned in 1 °C-wide intervals, for the whole data set. Regarding the LWP, values are binned in 0.2 g m^{-2}-wide intervals, for the whole data set. For each interval of time j from 1 to 48, a weighted average of h ($\overline{h_j}$), T ($\overline{T_j}$), and LWP ($\overline{LWP_j}$) is then calculated as:

$$\overline{x_j} = \frac{\sum_{i=1}^{M} N_{ij}\, x_{ij}}{\sum_{i=1}^{M} N_{ij}} \text{ with } x = h, T \text{ and } LWP. \quad (2)$$

4.2. Diurnal variation of SLW clouds vs height

The probability density (PD, %) of the height h of the SLW clouds (km) as a function of UTC Time t (Hour) in December 2018–2021 is presented in Fig. 13. We also show different statistics: 1) the mean height of SLW clouds as a function of t considering all the SLW clouds; 2) the number of SLW clouds as a function of t; and 3) the percentage of SLW clouds as a function of t. For each of these three statistics, we consider all the SLW clouds whatever their height (h > 0 m), SLW clouds above 325 m, below 325 m and below 100 m, except the cloud percentage for which the class containing all clouds is ignored.

On average, SLW clouds occur mainly in a quite steady, vertical domain ranging 400–600 m, between 06:00 and 15:00 UTC. Before and after this period, three other regimes are clearly identified. 1) From 15:00 to 24:00 UTC, the SLW clouds tend to decrease from 400 to 600 to 200 m, then 2) to increase from 200 to 400–600 m from 00:00 to 06:00 UTC. 3) From 18:00 to 24:00 UTC, another layer of SLW clouds is located below 100 m. These regimes deduced from the climatological sources are obviously consistent with the results deduced from the case study, namely the "entrainment zone" between 06:00 and 15:00 UTC, the residual conditions from 15:00 to 06:00 UTC, the downfall of the PBL to the top of the stable boundary layer from 15:00 to 24:00 UTC followed by the increase of the PBL top height to the top of the entrainment zone from 00:00 to 06:00 UTC, and the stable boundary layer from 18:00 to 24:00 UTC that contains liquid fog.

The diurnal variation of the SLW cloud height (h > 0 m) is mainly driven by the clouds located above 325 m (Fig. 13). Although the majority of SLW clouds are observed after 12:00 UTC, clouds above 325 m are mostly (>60 %) detected between 06:00 and 18:00 UTC while clouds below 100 m are mostly (>10 %) detected between 18:00 and 06:00 UTC.

In Fig. 14, we superimposed the diurnal cycle of the PBL shown in Fig. 13 (red line) on the PD of the SLW cloud height. We clearly see the three different regimes associated with the presence of SLW clouds. 1) Most of the SLW clouds are observed between 03:00 and 14:00 UTC in the entrainment zone, below the PBL top height and the capping temperature inversion. Although they have formed during the part of the day when a mixed layer – connected to the surface – exists, they can remain even when the stable surface layer introduces a decoupling from the surface. This area of clouds throughout the day is marked by the black rectangle in Fig. 14. 2) Liquid fog may form between 18:00 and 24:00 UTC within the stable boundary layer (white rectangle). And 3) higher SLW clouds may still be present, either as a remnant of the PBL which was present over the station one or more days earlier, or because they have been advected via long-range transport within a fossil cloud layer (yellow rectangle).

4.3. Diurnal variation of SLW clouds vs temperature

The probability density (PD, %) of the temperature (Celsius) as a function of UTC time t in the SLW clouds in December 2018–2021 is shown in Fig. 15. We also show different statistics regarding the mean temperature in the SLW clouds, the number of SLW clouds and the percentage of SLW clouds. For each of these statistics, we consider SLW clouds for temperatures greater than −40 °C, between −40 °C and −25 °C and greater than −25 °C, except the cloud percentage for which the class "greater than −40 °C″ is ignored.

SLW clouds over the Concordia station are mainly observed (>85 %) in a temperature range from −35 °C to −25 °C. Note that SLW can exist between 0 °C and −39 °C theoretically, although it has been observed in laboratory measurements down to −42.55 °C (Goy et al., 2018). The great majority of SLW clouds (>90 %) are observed from 16:00 UTC and during 11 h (i.e. including the 00:00–02:00 UTC period). SLW clouds observed for temperatures greater than −25 °C are not common (less than 10 % of the observations) except between 03:00 and 08:00 UTC when temperatures can reach −20 °C to −15 °C, representing about 15

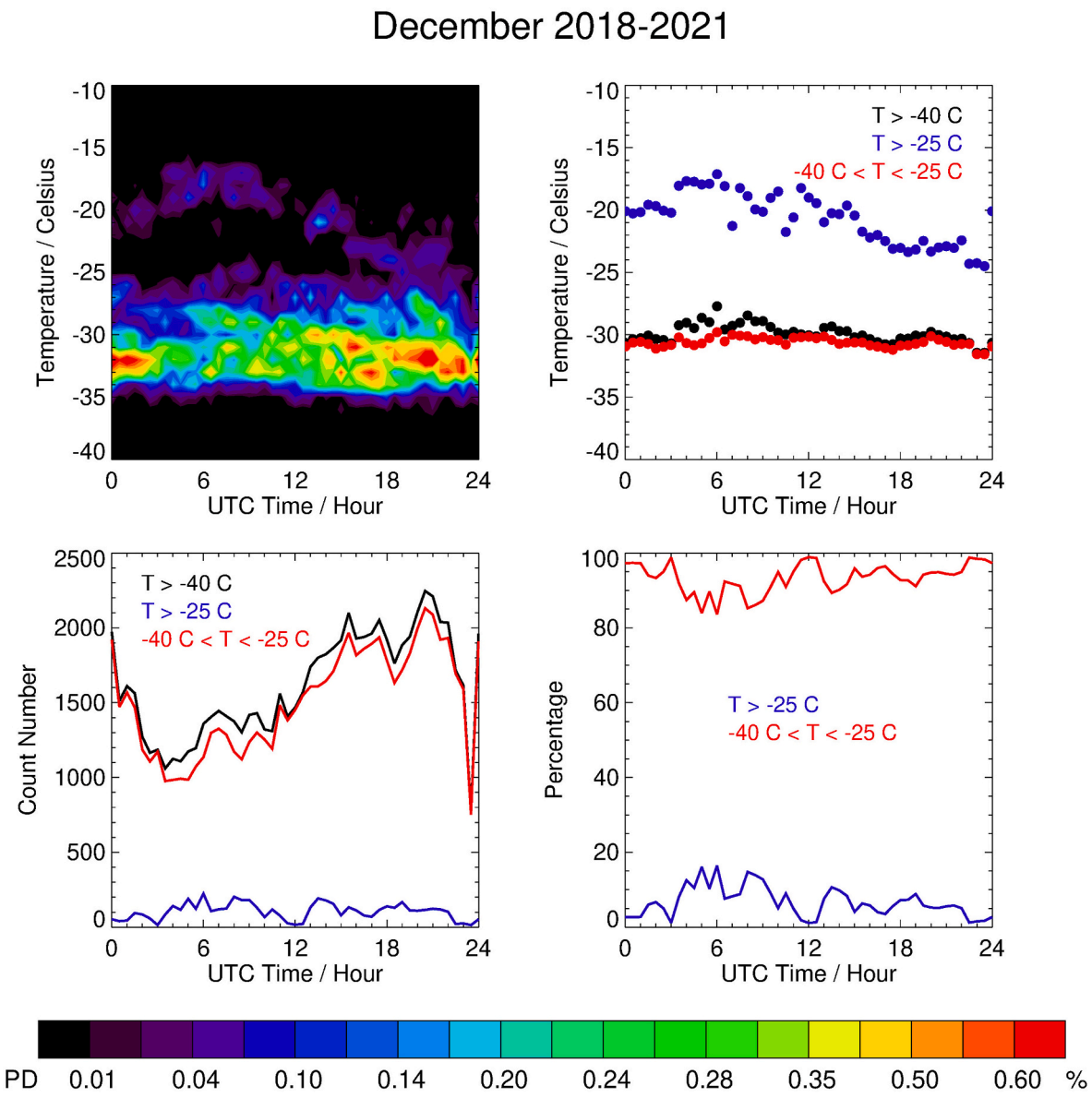

Fig. 15. Same as Fig. 13 but with temperature and temperature ranges (greater than −40 °C in black, between −40 °C and −25 °C in red and greater than −25 °C in blue) instead of height and height ranges, respectively. (For interpretation of the references to colour in this figure legend, the reader is referred to the Web version of this article.)

% of the observations. These warm episodes are usually associated with 1) the intrusion of oceanic-origin wet and warm air masses (see e.g. Ricaud et al., 2017) and/or 2) episodes of atmospheric rivers (see e.g. Wille et al., 2024a; and b).

4.4. Diurnal variation of SLW clouds vs LWP

The probability density (PD, %) of the LWP (g m^{-2}) as a function of UTC time *t* in the SLW clouds in December 2018–2021 is presented in Fig. 16. We also show different statistics regarding the mean LWP in the SLW clouds, the number of SLW clouds and the percentage of SLW clouds. For each of these statistics, we consider SLW clouds for LWPs greater than 0 g m^{-2}, less than 3 g m^{-2} and greater than 3 g m^{-2}, except the cloud percentage for which the class "greater than 0 g m^{-2}" is ignored.

SLW clouds over the Concordia station are mainly observed (>70 %) for LWP less than 3 g m^{-2}. There are some episodes of SLW clouds with large LWPs (>10 g m^{-2}) usually associated with 1) the intrusion of oceanic-origin wet and warm air masses and/or 2) episodes of atmospheric rivers, but this is not common (<5 %). Most of SLW clouds (>90 %), whatever the amount of LWP (greater or less than 3 g m^{-2}), are observed from 16:00 UTC and during 11 h (i.e. including the 00:00–02:00 UTC period), which is consistent with the analysis according to temperature presented above.

4.5. Synthesis of the climatological study

The diurnal evolution of the SLW clouds in the climatological study is consistent with the results obtained in the case study. The three regimes are also well depicted in the climatological data sets with SLW clouds present: 1) at the top of the PBL between the entrainment zone and the capping inversion layer, 2) higher up within a fossil layer and 3) within the very cold stable boundary layer close to the surface. In addition, as a key result from this climatological analysis, we can state that, although the time frame 06:00–14:00 UTC represents the main period when SLW clouds form into the entrainment zone (400–600 m), the time frame from 18:00 UTC and lasting 9 h is the outstanding period to observe SLW clouds both below the capping temperature inversion layer (400–600 m)

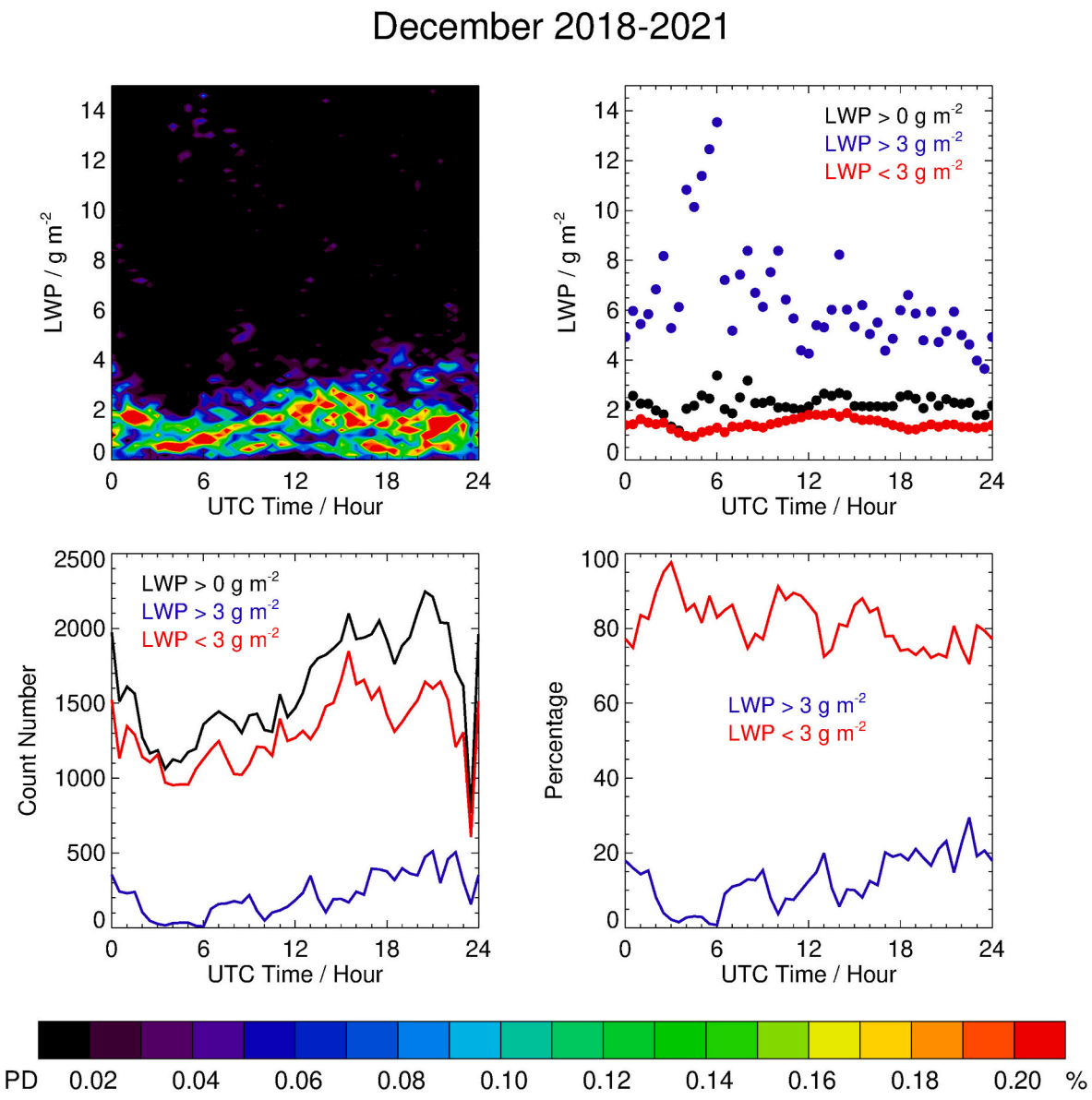

Fig. 16. Same as Fig. 13 but with LWP and LWP ranges (greater than 0 g m^{-2} in black, less than 3 g m^{-2} in red and greater than 3 g m^{-2} in blue) instead of height and height ranges, respectively. (For interpretation of the references to colour in this figure legend, the reader is referred to the Web version of this article.)

and within the stable boundary layer (<100 m) as liquid fog.

5. Conclusions

Based on the analysis of observations performed 1) during a single day (January 23, 2023) as a case study and 2) over four months of December (2018–2021) as a climatological study, our results show a consistent view of the diurnal variation of the PBL impacting the formation of SLW clouds and, to a lesser extent, liquid fog over the Concordia station (Antarctica) in summer. Observations based on remote-sensing instruments (HAMSTRAD and LIDAR) and in situ meteorological sondes provide a large data set to describe the diurnal cycle of temperature, relative humidity, LWP and SLW clouds.

We found that SLW clouds are essentially present when temperatures exhibit a local minimum and a relative humidity local maximum (>85 %) following three regimes: 1) at the top of the PBL between the entrainment zone and the capping inversion layer, 2) higher up within a fossil layer and 3) within the very cold stable boundary layer close to the surface. The SLW clouds in the fossil layer are either advected via long-range transport or a remnant of the PBL present over the station one or more days earlier. Liquid fog generally develops within the very cold stable boundary layer.

The majority of SLW clouds are present in the (active or residual) entrainment zone between 400 and 600 m from 06:00 to 14:00 UTC (from 14:00 to 22:00 LT). The liquid fog within the stable boundary layer is essentially detected below 100 m during the very low temperature period from 18:00 UTC during a period of 9 h (from 02:00 to 10:00 LT). The SLW clouds in the fossil layer can, by definition, be detected at any height but statistically they are present above the first inflexion point in the θ profile, in a 600–900 m height range and from 00:00 to 24:00 UTC.

The in-cloud temperature is ranging from −35 °C to −25 °C for LWPs less than 3.0 g m^{-2}. Some SLW clouds associated with in-cloud temperatures greater than −25 °C (reaching −18 °C) and LWPs greater than 3.0 g m^{-2} (reaching up to 14.0 g m^{-2}) are rarely detected and usually associated with 1) the intrusion of oceanic-origin wet and warm air masses and/or 2) episodes of atmospheric rivers.

In the case study, we compared the outputs from the ARPEGE NWP and the ERA5 reanalyses with our observations and findings. The water liquid-ice partition function in ARPEGE settings has been modified in

favour of liquid water for temperatures less than 0 °C. ARPEGE and ERA5 highlighted the presence of SLW clouds with some large differences with observations. ARPEGE showed a too warm (by 5 °C) and wet (by 10 % in relative humidity) atmosphere producing far too much ice and SLW clouds. ERA5 temperature was consistent with observations but ERA5 relative humidity showed a high bias of about 30 % with observations producing supersaturation reaching 110 %. Due to the low vertical resolution (~500 m) and the absence of a PBL, a SLW cloud appeared only once and far too high (~1200 m). The PBL top height calculated by ARPEGE and ERA5 was consistent with the one deduced from observations at the level of the inflection point in the potential temperature profile (200–300 m). Improvements in the vertical resolution and in the liquid-ice partition function of the models are the two major points in order to simulate realistic SLW clouds above the Antarctic plateau.

The present study based on remote-sensing observations of SLW clouds is being complemented by in-situ observations of SLW clouds through balloon-borne and drone-borne sondes. These new observations performed with drones will potentially add information on SLW clouds by increasing the vertical, horizontal and time resolutions.

CRediT authorship contribution statement

Philippe Ricaud: Writing – review & editing, Writing – original draft, Visualization, Validation, Supervision, Software, Methodology, Investigation, Funding acquisition, Formal analysis, Conceptualization. **Pierre Durand:** Writing – review & editing, Writing – original draft, Validation, Methodology, Investigation, Formal analysis. **Paolo Grigioni:** Writing – review & editing, Writing – original draft, Visualization, Validation, Methodology, Formal analysis. **Virginia Ciardini:** Writing – review & editing, Writing – original draft, Validation, Methodology, Formal analysis. **Massimo Del Guasta:** Writing – review & editing, Writing – original draft, Visualization, Validation, Methodology, Investigation, Formal analysis, Data curation. **Giuseppe Camporeale:** Writing – review & editing, Writing – original draft, Data curation. **Jean-Luc Attié:** Writing – review & editing, Writing – original draft, Validation, Conceptualization. **Eric Bazile:** Writing – review & editing, Writing – original draft, Validation, Data curation, Conceptualization.

Declaration of competing interest

The authors declare that they have no known competing financial interests or personal relationships that could have appeared to influence the work reported in this paper.

Acknowledgments

The HAMSTRAD programme (910) and the SLW-CLOUDS programme (1247) were supported by the French Polar Institute (IPEV), the Institut National des Sciences de l'Univers (INSU)/Centre National de la Recherche Scientifique (CNRS), Météo-France and the Centre National d'Etudes Spatiales (CNES). The permanently staffed Concordia station is jointly operated by IPEV and the Italian Programma Nazionale Ricerche in Antartide (PNRA). The tropospheric LIDAR operates at Dome C from 2008 within the framework of several Italian national (PNRA) projects. Meteorological radiosonde launches and the ceilometer are operated within the framework of the Italian Antarctic Meteorological Observatory (IAMCO) of the PNRA. We would like to thank all the winter over personnel who worked at Dome C on the different projects: HAMSTRAD, aerosol LIDAR, and IAMCO for operational meteorological soundings and in situ balloon-borne observations. Finally, we would like to thank the two anonymous reviewers for their beneficial comments.

Data availability

HAMSTRAD data are available at http://www.cnrm.meteo.fr/spip.php?article961&lang=en (last access: June 17, 2025). The tropospheric depolarization LIDAR data are reachable at http://lidarmax.altervista.org/lidar/Antarctic%20LIDAR.php (last access: June 17, 2025). Radiosondes and ceilometer data are available at http://www.climantartide.it (last access: June 17, 2025).

References

Bergeron, T., 1928. Über die dreidimensional verknüpfende Wetteranalyse. Geophys. Norv. (in German).

Bodas-Salcedo, A., Hill, P.G., Furtado, K., Williams, K.D., Field, P.R., Manners, J.C., et al., 2016. Large contribution of supercooled liquid clouds to the solar radiation budget of the Southern Ocean. J. Clim. 29 (11), 4213–4228. https://doi.org/10.1175/jcli-d-15-0564.1.

Bromwich, D.H., Nicolas, J.P., Hines, K.M., Kay, J.E., Key, E.L., Lazzara, Lubin, D., McFarquhar, G.M., Gorodetskaya, I.V., Grosvenor, D.P., Lachlan-Cope, T., van Lipzig, N.P.M., 2012. Tropospheric clouds in Antarctica. Rev. Geophys. 50, RG1004. https://doi.org/10.1029/2011RG000363.

Bromwich, D.H., Otieno, F.O., Hines, K.M., Manning, K.W., Shilo, E., 2013. Comprehensive evaluation of polar weather research and forecasting model performance in the antarctic. J. Geophys. Res. Atmos. 118, 274–292.

Choi, Y.S., Ho, C.H., Park, C.E., Storelvmo, T., Tan, I., 2014. Influence of cloud phase composition on climate feedbacks. J. Geophys. Res. Atmos. 119 (7), 3687–3700. https://doi.org/10.1002/2013jd020582.

Cossich, W., Maestri, T., Magurno, D., Martinazzo, M., Di Natale, G., Palchetti, L., Bianchini, G., Del Guasta, M., 2021. Ice and mixed-phase cloud statistics on the Antarctic Plateau. Atmos. Chem. Phys. 21, 13811–13833. https://doi.org/10.5194/acp-21-13811-2021.

Del Guasta, M., Ricaud, P., Scarchilli, C., Dreossi, G., 2024. A statistical study of precipitation on the eastern Antarctic plateau (Dome-C) using remote sensing and in-situ instrumentation. Polar Sci. https://doi.org/10.1016/j.polar.2024.101106.

Findeisen, W., 1938. Kolloid-meteorologische Vorgänge bei Niederschlagsbildung. In: Volken, E.A.M., Giesche, S., Brönnimann, Meteorol, Z. (Eds.), Meteorol. Z. 55, 121–133. https://doi.org/10.1127/metz/2015/0675 (in German).

Forbes, R.M., Ahlgrimm, M., 2014. On the representation of high-latitude boundary layer mixed-phase cloud in the ECMWF global model. Monthly Weather Review 142 (9), 3425–3445.

Goy, C., Potenza, M.A., Dedera, S., Tomut, M., Guillerm, E., Kalinin, A., Voss, K.-O., Schottelius, A., Petridis, N., Prosvetov, A., Tejeda, G., Fernández, J.M., Trautmann, C., Caupin, F., Glasmacher, U., Grisenti, R.E., 2018. Shrinking of rapidly evaporating water microdroplets reveals their extreme supercooling. Phys. Rev. Lett. 120, 015501. https://doi.org/10.1103/PhysRevLett.120.015501.

Grosvenor, D.P., Choularton, T.W., Lachlan-Cope, T., Gallagher, M.W., Crosier, J., Bower, K.N., Ladkin, R.S., Dorsey, J.R., 2012. In-situ aircraft observations of ice concentrations within clouds over the Antarctic Peninsula and larsen ice shelf. Atmos. Chem. Phys. 12, 11275–11294. https://doi.org/10.5194/acp-12-11275-2012.

Hersbach, H., Bell, B., Berrisford, P., Hirahara, S., Horányi, A., Muñoz-Sabater, J., Nicolas, J., Peubey, C., Radu, R., Schepers, D., Simmons, A., et al., 2020. The ERA5 global reanalysis. Q. J. R. Meteorol. Soc. 146 (730), 1999–2049.

Hogan, R.J., Illingworth, A.J., 2003. The Effect of Specular Reflection on Spaceborne Lidar Measurements of Ice Clouds, Report of the ESA Retrieval Algorithm for EarthCARE Project, p. 5.

King, J.C., Argentini, S.A., Anderson, P.S., 2006. Contrasts between the summertime surface energy balance and boundary layer structure at dome C and halley stations, Antarctica. J. Geophys. Res. Atmos. 111, D02105. https://doi.org/10.1029/2005JD006130.

King, J.C., Gadian, A., Kirchgaessner, A., Kuipers Munneke, P., Lachlan-Cope, T.A., Orr, A., Reijmer, C., Broeke, M.R., van Wessem, J.M., Weeks, M., 2015. Validation of the summertime surface energy budget of larsen C ice shelf (Antarctica) as represented in three high-resolution atmospheric models. J. Geophys. Res. Atmos. 120, 1335–1347. https://doi.org/10.1002/2014JD022604.

Komurcu, M., Storelvmo, T., Tan, I., Lohmann, U., Yun, Y., Penner, J.E., et al., 2014. Intercomparison of the cloud water phase among global climate models. J. Geophys. Res. Atmos. 119 (6), 3372–3400. https://doi.org/10.1002/2013jd021119.

Lachlan-Cope, T., 2010. Antarctic clouds. Polar Res. 29, 150–158.

Lachlan-Cope, T., Listowski, C., O'Shea, S., 2016. The microphysics of clouds over the Antarctic peninsula – part 1: observations. Atmos. Chem. Phys. 16, 15605–15617. https://doi.org/10.5194/acp-16-15605-2016.

Lawson, R.P., Gettelman, A., 2014. Impact of Antarctic mixed-phase clouds on climate. P. Natl. Acad. Sci. USA 111, 18156–18161.

Lemus, L., Rikus, L., Martin, C., Platt, R., 1997. Global cloud liquid water path simulations. J. Clim. 10 (1), 52–64.

Lenaerts, J.T., Van Tricht, K., Lhermitte, S., L'Ecuyer, T.S., 2017. Polar clouds and radiation in satellite observations, reanalyses, and climate models. Geophys. Res. Lett. 44 (7), 3355–3364.

Listowski, C., Lachlan-Cope, T., 2017. The microphysics of clouds over the Antarctic Peninsula – part 2: modelling aspects within polar WRF. Atmos. Chem. Phys. 17, 10195–10221. https://doi.org/10.5194/acp-17-10195-2017.

Listowski, C., Delanoë, J., Kirchgaessner, A., Lachlan-Cope, T., King, J., 2019. Antarctic clouds, supercooled liquid water and mixed phase, investigated with DARDAR: geographical and seasonal variations. Atmos. Chem. Phys. 19, 6771–6808. https://doi.org/10.5194/acp-19-6771-2019.

Lubin, D., Chen, B., Bromwich, D.H., Somerville, R.C., Lee, W.H., Hines, K.M., 1998. The impact of antarctic cloud radiative properties on a GCM climate simulation. J. Clim. 11, 447–462.

McCoy, D.T., Hartmann, D.L., Zelinka, M.D., Ceppi, P., Grosvenor, D.P., 2015. Mixed-phase cloud physics and Southern Ocean cloud feedback in climate models. J. Geophys. Res. Atmos. 120 (18), 9539–9554. https://doi.org/10.1002/2015jd023603.

Mishchenko, M.I., Hovenier, J.W., Travis, L.D. (Eds.), 2000. Light Scattering by Nonspherical Particles: Theory, Measurements, and Applications. Academic Press, pp. 393–416 chap. 14.

Pailleux, J., Geleyn, J.-F., El Khatib, R., Fischer, C., Hamrud, M., Thépaut, J.-N., Rabier, F., Andersson, E., Salmond, D., Burridge, D., Simmons, A., Courtier, P., 2015. Les 25 ans du système de prévision numérique du temps IFS/Arpège. La Météorologie 89, 18–27. https://doi.org/10.4267/2042/56594 (in French).

Ricaud, P., Gabard, B., Derrien, S., Chaboureau, J.-P., Rose, T., Mombauer, A., Czekala, H., 2010. HAMSTRAD-Tropo, A 183-GHz radiometer dedicated to sound tropospheric water vapor over concordia station, Antarctica. IEEE T. Geosci. Remote 48, 1365–1380. https://doi.org/10.1109/TGRS.2009.2029345.

Ricaud, P., Genthon, C., Attié, J.-L., Carminati, F., Canut, G., Durand, P., Vanacker, J.-F., Moggio, L., Courcoux, Y., Pellegrini, A., Rose, T., 2012. Summer to Winter Diurnal Variabilities of Temperature and Water Vapour in the lowermost troposphere as observed by HAMSTRAD over Dome C Antarctica. Boundary-Layer Meteorology. Vol. 143, N° 1, pp. 227-259, DOI: 10.1007/s10546-011-9673-6.

Ricaud, P., Bazile, E., del Guasta, M., Lanconelli, C., Grigioni, P., Mahjoub, A., 2017. Genesis of diamond dust, ice fog and thick cloud episodes observed and modelled above dome C, Antarctica. Atmos. Chem. Phys. 17, 5221–5237. https://doi.org/10.5194/acp-17-5221-2017.

Ricaud, P., Del Guasta, M., Bazile, E., Azouz, N., Lupi, A., Durand, P., Attié, J.-L., Veron, D., Guidard, V., Grigioni, P., 2020. Supercooled liquid water cloud observed, analysed, and modelled at the top of the planetary boundary layer above dome C, Antarctica. Atmos. Chem. Phys. 20, 4167–4191. https://doi.org/10.5194/acp-20-4167-2020.

Ricaud, P., Del Guasta, M., Lupi, A., Roehrig, R., Bazile, E., Durand, P., Attié, J.-L., Nicosia, A., Grigioni, P., 2024a. Supercooled liquid water clouds observed over dome C, Antarctica: temperature sensitivity and cloud radiative forcing. Atmos. Chem. Phys. 24, 613–630. https://doi.org/10.5194/acp-24-613-2024.

Ricaud, P., Durand, P., Grigioni, P., Del Guasta, M., Camporeale, G., Roy, A., Attié, J.-L., Bognar, J., 2024b. In situ observations of supercooled liquid water clouds over dome C, Antarctica, by balloon-borne sondes. Atmos. Meas. Tech. 17, 5071–5089. https://doi.org/10.5194/amt-17-5071-2024.

Ricaud, P., 2025. ERA5 deficit in supercooled liquid water cloud radiative forcing at dome C, Antarctica. Q. J. R. Meteorol. Soc. revised, QJ-25-0111.

Silber, I., Verlinde, J., Cadeddu, M., Flynn, C.J., Vogelmann, A.M., Eloranta, E.W., 2019. Antarctic cloud macrophysical, thermodynamic phase, and atmospheric inversion coupling properties at McMurdo station—part II: radiative impact during different synoptic regimes. J. Geophys. Res. Atmos. 124, 1697–1719. https://doi.org/10.1029/2018JD029471.

Storelvmo, T., 2017. Aerosol effects on climate via mixed-phase and ice clouds. Annu. Rev. Earth Planet Sci. 45, 199–222. https://doi.org/10.1146/annurev-earth-060115-012240.

Storelvmo, T., Tan, I., 2015. The wegener–bergeron–findeisen process—Its discovery and vital importance for weather and climate. Meteoros 24, 455–461. Z.

Stull, R.B., 2012. An Introduction to Boundary Layer Meteorology, 13. Springer Science & Business Media.

Tetzner, D., Thomas, E., Allen, C., 2019. A validation of ERA5 reanalysis data in the Southern antarctic Peninsula—Ellsworth land region, and its implications for ice core studies. Geosciences 9, 289. https://doi.org/10.3390/geosciences9070289.

Tsushima, Y., Emori, S., Ogura, T., Kimoto, M., Webb, M.J., Williams, K.D., et al., 2006. Importance of the mixed-phase cloud distribution in the control climate for assessing the response of clouds to carbon dioxide increase: a multi-model study. Clim. Dyn. 27 (2), 113–126. https://doi.org/10.1007/s00382-006-0127-7.

Vignon, É., Alexander, S.P., DeMott, P.J., Sotiropoulou, G., Gerber, F., Hill, T.C.J., Marchand, R., Nenes, A., Berne, A., 2021. Challenging and improving the simulation of mid-level mixed-phase clouds over the high-latitude Southern Ocean. J. Geophys. Res. 126, e2020JD033490. https://doi.org/10.1029/2020JD033490.

Wang, Y., Li, J., Zhao, Y., Li, Y., Zhao, Y., Wu, X., 2022. Distinct diurnal cycle of supercooled water cloud fraction dominated by dust extinction coefficient. Geophys. Res. Lett. 49, e2021GL097006. https://doi.org/10.1029/2021GL097006.

Wegener, A., 1911. Thermodynamik Der Atmosphäre. Barth, Leipzig, Germany (in German).

Wille, J.D., Alexander, S.P., Amory, C., Baiman, R., Barthélemy, L., Bergstrom, D.M., Berne, A., Binder, H., Blanchet, J., Bozkurt, D., Bracegirdle, T.J., et al., 2024a. The extraordinary march 2022 East Antarctica heat wave. Part I: observations and meteorological drivers. J. Clim. 37 (3), 757–778. https://doi.org/10.1175/JCLI-D-23-0175.1.

Wille, J.D., Alexander, S.P., Amory, C., Baiman, R., Barthélemy, L., Bergstrom, D.M., Berne, A., Binder, H., Blanchet, J., Bozkurt, D., Bracegirdle, T.J., et al., 2024b. The extraordinary march 2022 East Antarctica “heat” wave. Part II: impacts on the Antarctic ice sheet. J. Clim. 37 (3), 779–799. https://doi.org/10.1175/JCLI-D-23-0176.1.

Young, G., Lachlan-Cope, T., O’Shea, S.J., Dearden, C., Listowski, C., Bower, K.N., Choularton, T.W., Gallagher, M.W., 2019. Radiative effects of secondary ice enhancement in coastal Antarctic clouds. Geophys. Res. Lett. 46, 2312–2321. https://doi.org/10.1029/2018GL080551.

Zhang, D., Vogelmann, A., Kollias, P., Luke, E., Yang, F., Lubin, D., Wang, Z., 2019. Comparison of Antarctic and arctic single-layer stratiform mixed-phase cloud properties using ground-based remote sensing measurements. J. Geophys. Res. Atmos. 124 (17–18), 10186–10204. https://doi.org/10.1029/2019JD030673.